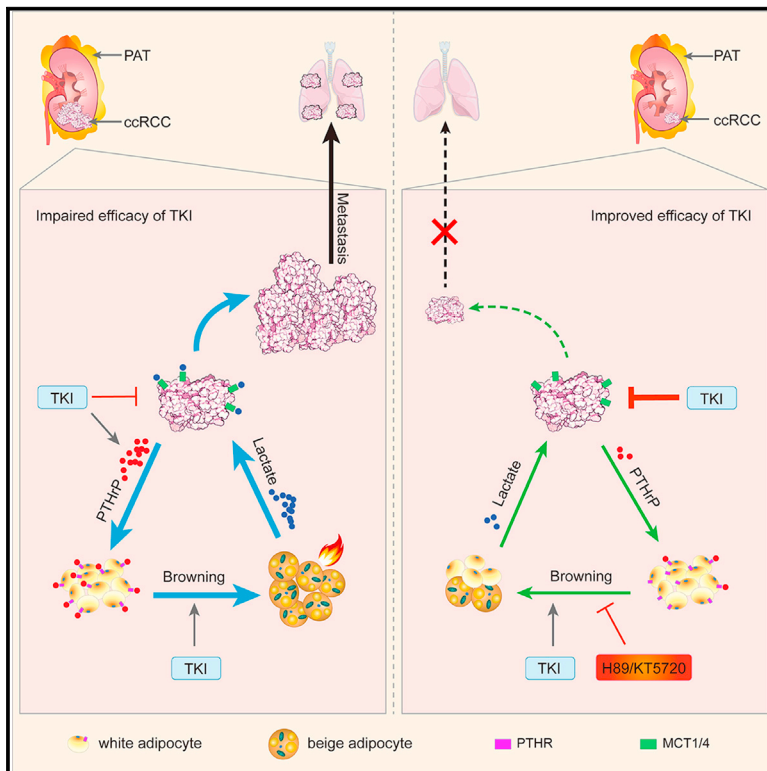# The thermogenic activity of adjacent adipocytes fuels the progression of ccRCC and compromises anti-tumor therapeutic efficacy

Graphical abstract

Authors

Gang Wei, Honglin Sun, Kai Dong, ..., Xiaoyong Hu, Linhui Wang, Junli Liu

Correspondence

wanglinhui@smmu.edu.cn (L.W.), liujunli@sjtu.edu.cn (J.L.)

In brief

Wei et al. report that bi-directional communication between ccRCC tumor cells and adjacent perinephric adipose tissue promotes the browning of the latter and the growth, invasion, and metastasis of the former. They reveal that combination treatment with the tyrosine kinase inhibitor sunitinib and a thermogenic inhibitor (H89 or KT5720) synergistically augments anti-tumor activity.

Highlights

- ccRCC-secreted PTHrP promotes the browning of adjacent adipocytes via PKA

- During such browning excess lactate is released, promoting ccRCC tumor progression

- Blocking ccRCC-adipocyte communication inhibits tumor growth, invasion, and metastasis

- Pharmacological inhibition of local browning enhances anti-tumor efficacy

CelPress

Cell Metabolism

CellPress

Article

The thermogenic activity of adjacent adipocytes fuels the progression of ccRCC and compromises anti-tumor therapeutic efficacy

Gang Wei,[1,8] Honglin Sun,[1,8] Kai Dong,[2,8] Libing Hu,[3,8] Qi Wang,[4,8] Qian Zhuang,[5,8] Yan Zhu,[2,8] Xianjing Zhang,[1] Yaodi Shao,[1] Huiru Tang,[4] Zhenfei Li,[5] Suzhen Chen,[1] Junxi Lu,[1] Yibing Wang,[6] Xinxin Gan,[2] Tao P. Zhong,[7] Dingkun Gui,[1] Xiaoyong Hu,[1] Linhui Wang,[2,*] and Junli Liu[1,9,*]

[1]Shanghai Diabetes Institute, Department of Endocrinology and Metabolism, Shanghai Jiao Tong University Affiliated Sixth People's Hospital, Key Laboratory of Cell Differentiation and Apoptosis of the Chinese Ministry of Education, Shanghai Jiao Tong University School of Medicine, Shanghai 200032, China
[2]Department of Urology, Changhai Hospital, Naval Medical University, Shanghai 200433, China
[3]Department of Urology, Yan'an Affiliated Hospital of Kunming Medical University, Kunming, Yunnan 650051, China
[4]State Key Laboratory of Genetic Engineering, School of Life Sciences, Human Phenome Institute, Metabonomics and Systems Biology Laboratory at Shanghai International Centre for Molecular Phenomics, Zhongshan Hospital, Fudan University, Shanghai 200438, China
[5]State Key Laboratory of Cell Biology, CAS Center for Excellence in Molecular Cell Science, Shanghai Institute of Biochemistry and Cell Biology, Chinese Academy of Sciences, Shanghai 200031, China
[6]School of Kinesiology, Shanghai University of Sport, Shanghai 200438, China
[7]Shanghai Key Laboratory of Regulatory Biology, School of Life Sciences, East China Normal University, Shanghai 200241, China
[8]These authors contributed equally
[9]Lead contact
*Correspondence: wanglinhui@smmu.edu.cn (L.W.), liujunli@sjtu.edu.cn (J.L.)
https://doi.org/10.1016/j.cmet.2021.08.012

SUMMARY

Clear cell renal cell carcinoma (ccRCC) preferentially invades into perinephric adipose tissue (PAT), a process associated with poor prognosis. However, the detailed mechanisms underlying this interaction remain elusive. Here, we describe a bi-directional communication between ccRCC cells and the PAT. We found that ccRCC cells secrete parathyroid-hormone-related protein (PTHrP) to promote the browning of PAT by PKA activation, while PAT-mediated thermogenesis results in the release of excess lactate to enhance ccRCC growth, invasion, and metastasis. Further, tyrosine kinase inhibitors (TKIs) extensively used in the treatment of ccRCC enhanced this vicious cycle of ccRCC-PAT communication by promoting the browning of PAT. However, if this cross-communication was short circuited by the pharmacological suppression of adipocyte browning via H89 or KT5720, the anti-tumor efficacy of the TKI, sunitinib, was enhanced. These results suggest that ccRCC-PAT cross-communication has important clinical relevance, and use of combined therapy holds great promise in enhancing the efficacy of TKIs.

INTRODUCTION

Renal cell carcinoma (RCC) is a frequently lethal malignancy that accounts for more than 2% of all adult cancers (Zarrabi et al., 2017). Based on histological and cytogenetic signatures, 80% of RCC is subcategorized as clear cell renal cell carcinoma (ccRCC) (Zarrabi et al., 2017; Xu and Wu, 2015). Perinephric adipose tissue (PAT) is a type of white adipose tissue (WAT) found between the renal fascia and renal capsule, which surrounds the kidney and supports its function (Okhunov et al., 2012). During tumorigenesis, ccRCC cells can infiltrate through the kidney capsule and into the PAT (Bedke et al., 2009), a process associated with poor prognosis (Shah et al., 2019). However, the detailed mechanisms behind these findings remain elusive.

Cancers can drive the metabolic reprogramming of adjacent non-cancerous cells (Fiaschi et al., 2012) to provide the additional energetic substrates and metabolites needed for rapid tumor growth. Although PAT is a key component of the renal tumor microenvironment, the interplay between ccRCC and PAT have not been well studied, which may be crucial for ccRCC growth and metastasis.

There is increasing evidence that several kinds of cancers drive WAT browning (Huang et al., 2016). WAT browning is typically marked by upregulated expression of uncoupling protein 1 (UCP1) and by mitochondrial biogenesis, which also enhance the cellular metabolism of adipocytes and the metabolites released by them (Petruzzelli et al., 2014). However, whether ccRCC could promote the browning of adjacent adipocytes in PAT and the putative PAT browning could contribute to ccRCC
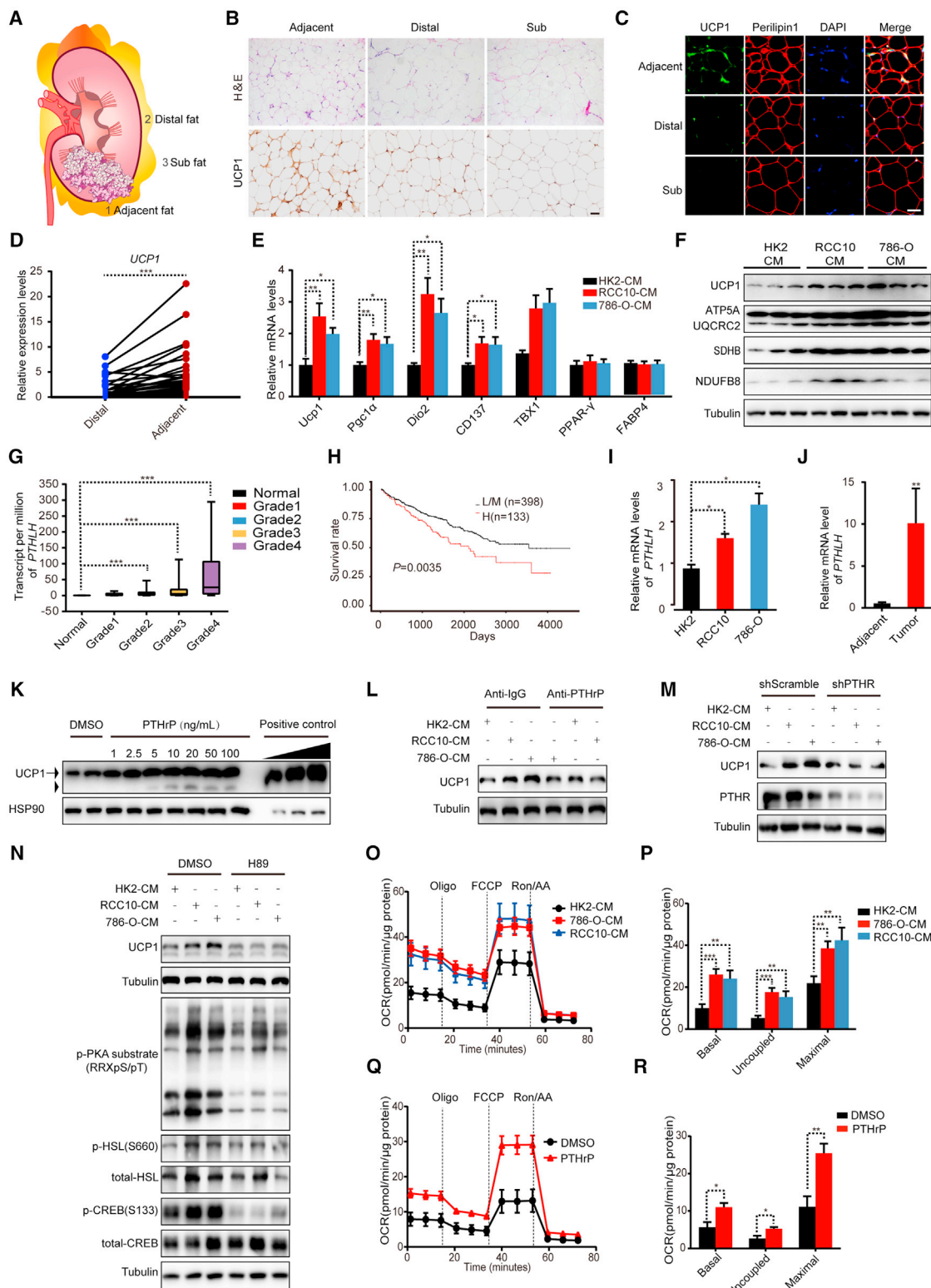
Figure 1. ccRCC tumor-derived PTHrP promotes PAT adipocyte browning

(A) Schematic diagram of ccRCC tumor and fat adherent to the tumor (adjacent) or farther away (>5 cm) from the tumor (distal). Subcutaneous fat (Sub) serves as a control.

(B) Representative images of H&E- (top row) (10 images per 5 biological replicates for each group) and IHC-stained (with an anti-UCP1 antibody) (bottom row) (10 images per 5 biological replicates for each group) sections of tumor-adjacent fat, distal fat, and sub fat. Scale bar, 50 μm.

(legend continued on next page)

growth and metastasis remain elusive. Tyrosine kinase inhibitors (TKIs) are widely used in the treatment of ccRCC (Tsao et al., 2017; Rini and Atkins, 2009). Yet there is evidence indicating that the therapeutic efficacy of TKIs is compromised under some conditions (Rini and Atkins, 2009). So far, the widely accepted view is that impaired TKI efficacy owes to the reestablishment of tumor neo-vascularization triggered via redundant VEGFR-dependent and -independent pathways (De Palma et al., 2017). However, other factors limiting TKI efficacy are still underappreciated. Whether and how TKIs affect the communication between ccRCCs and adjacent adipocytes is still unclear and is an important question in ccRCC-related therapies.

In this study, we compared WAT samples surrounding human ccRCCs and found evidence of marked browning in this tissue. Consequently, we delineated in detail a bi-directional communication between ccRCCs and PAT, revealing a tumor-supportive role of adjacent beige adipocytes in the ccRCC tumor microenvironment (TME). Intriguingly, we found that widely used TKIs strengthened adipocyte browning, which in turn promoted tumor growth, invasion, and metastasis, thus providing a mechanism to explain the decreased TKI efficacy in certain clinical situations.

RESULTS

PAT specimens adjacent to ccRCCs show evidence of browning

We collected clinical adipose tissue specimens (PAT and subcutaneous WAT) from individuals with ccRCC, and we categorized these samples in three ways: adipose tissue adherent to the tumor (adjacent), adipose tissue more than 5 cm from the tumor site (distal), and subcutaneous adipose tissue (sub) (Figure 1A). We stained these samples by hematoxylin and eosin (H&E) and found that adipocytes in adjacent fat were smaller than adipocytes in distal fat samples from the same individuals (Figures 1B and S1A). Moreover, we performed immunohistochemistry and immunofluorescence staining and found that tumor-adjacent adipocytes had higher expression of uncoupling protein 1 (UCP1) than adipocytes in distal fat (Figures 1B, 1C, and S1B). We also found that the upregulated UCP1 fluorescence in tumor-adjacent adipocytes overlapped well with the adipocyte-specific marker Perilipin1 (Figure 1C), further confirming that the PAT adherent to the ccRCCs underwent a browning process.

With broader analysis of gene expression, we found that multiple browning markers were greater in adjacent versus distal fat, including UCP1 (Figure 1D), as well as PGC1α, CIDEα, DIO2, and TBX1 (Figures S1C–S1F). In contrast, the mRNA abundances of the white adipose markers LEPTIN and SHOX2 were lower in adjacent fat compared with distal fat (Figures S1G and S1H), while the expression of the pan-adipocyte marker FABP4 was equivalent in both fat samples (Figure S1I). We also found that the copy number of mitochondrial DNA in adjacent fat was significantly higher than that in distal fat (p < 0.05) (Figure S1J).

ccRCC-secreted PTHrP promotes browning of the adjacent PAT

To determine whether ccRCC induces browning of the PAT, we collected culture media from two ccRCC cell lines (786-O and RCC10) and one normal renal cell line (HK2), which we used to treat white adipocytes differentiated from C3H10T1/2 cells or primary pre-adipocytes isolated from subcutaneous WAT (Figure S1K). The expression levels of genes involved in browning, including Ucp1, Pgc1α, and Dio2, were remarkably higher in murine adipocytes (differentiated C3H10T1/2) treated with ccRCC cell conditioned medium (CM) than in those treated with media from HK2 cells (Figures 1E and S1L). Further, we confirmed that ccRCC cell CM increased the abundance of UCP1 and other

(C) Immunofluorescent detection of UCP1 and Perilipin1 in tumor-adjacent, distal, and sub fat of individuals with ccRCC (10 images per 5 biological replicates for each group). Scale bar, 50 μm.

(D) mRNA levels of UCP1 in 54 paired adjacent and distal fat samples from individuals with ccRCC (1 technical replicate of 54 biological replicates per group).

(E) Expression levels of pan-adipocyte markers and browning-related genes in differentiated C3H10T1/2 cells after treatment with the CM from HK2, RCC10, or 786-O cells for 24 h (1 technical replicate of 4 biological replicates per group).

(F) Immunoblots of UCP1 and mitochondrial proteins in differentiated C3H10T1/2 cell treatment with the CM from HK2, RCC10, or 786-O cells for 24 h (n = 3; representative of 3 biological replicates per group).

(G) mRNA levels of PTHLH in normal study participants (n = 72) or individuals with ccRCC (grade 1, n = 14; grade 2, n = 229; grade 3, n = 206; and grade 4, n = 76) according to TCGA database.

(H) The association of PTHLH mRNA levels and the survival rate of individuals with ccRCC, based on TCGA database.

(I) PTHLH mRNA levels in HK2, RCC10, and 786-O cells (1 technical replicate of 4 biological replicates per group).

(J) PTHLH mRNA levels in paired normal and ccRCC samples (1 technical replicate of 28 biological replicates per group).

(K) Immunoblots of UCP1 in differentiated C3H10T1/2 cells after treatment with indicated concentrations of PTHrP for 24 h (n = 2; representative of 2 biological replicates per group). Arrow indicates the UCP1 protein band and arrowhead marks unspecific band.

(L) Immunoblots of UCP1 in differentiated C3H10T1/2 cells treated with the CM from HK2, RCC10, or 786-O cells in the presence of neutralizing anti-PTHrP antibody or control IgG for 24 h (n = 2; representative of 2 biological replicates per group).

(M) Representative immunoblots of UCP1 in differentiated shPTHR or shScramble C3H10T1/2 cells after treatment with CM from HK2, RCC10, or 786-O cells for 24 h (n = 2; representative of 2 biological replicates in total).

(N) Immunoblots of phosphorylated PKA substrates, p-HSL (S660), total HSL, p-CREB (S133), and total CREB in differentiated C3H10T1/2 cells with different treatments as shown for 24 h (n = 1 in total).

(O) OCR of differentiated C3H10T1/2 cells was determined by Seahorse after treatment with CM from HK2, RCC10, or 786-O cells for 24 h (1 technical replicate of 9–10 biological replicates per group).

(P) Basal, uncoupled, and maximal OCR from Seahorse in (O) (1 technical replicate of 9–10 biological replicates per group).

(Q) OCR of differentiated C3H10T1/2 cells was determined by Seahorse after treatment with PTHrP for 24 h (1 technical replicate of 6 biological replicates per group).

(R) Basal, uncoupled, and maximal OCR from Seahorse in (Q) (1 technical replicate of 6 biological replicates per group).

Data were expressed as means ± SEM or median (G). *p < 0.05, **p < 0.01, ***p < 0.001 by paired two-tailed Student's t test (D), one-way ANOVA (E, I, and P), t test (G), log-rank test (H), or unpaired two-tailed Student's t test (J and R).
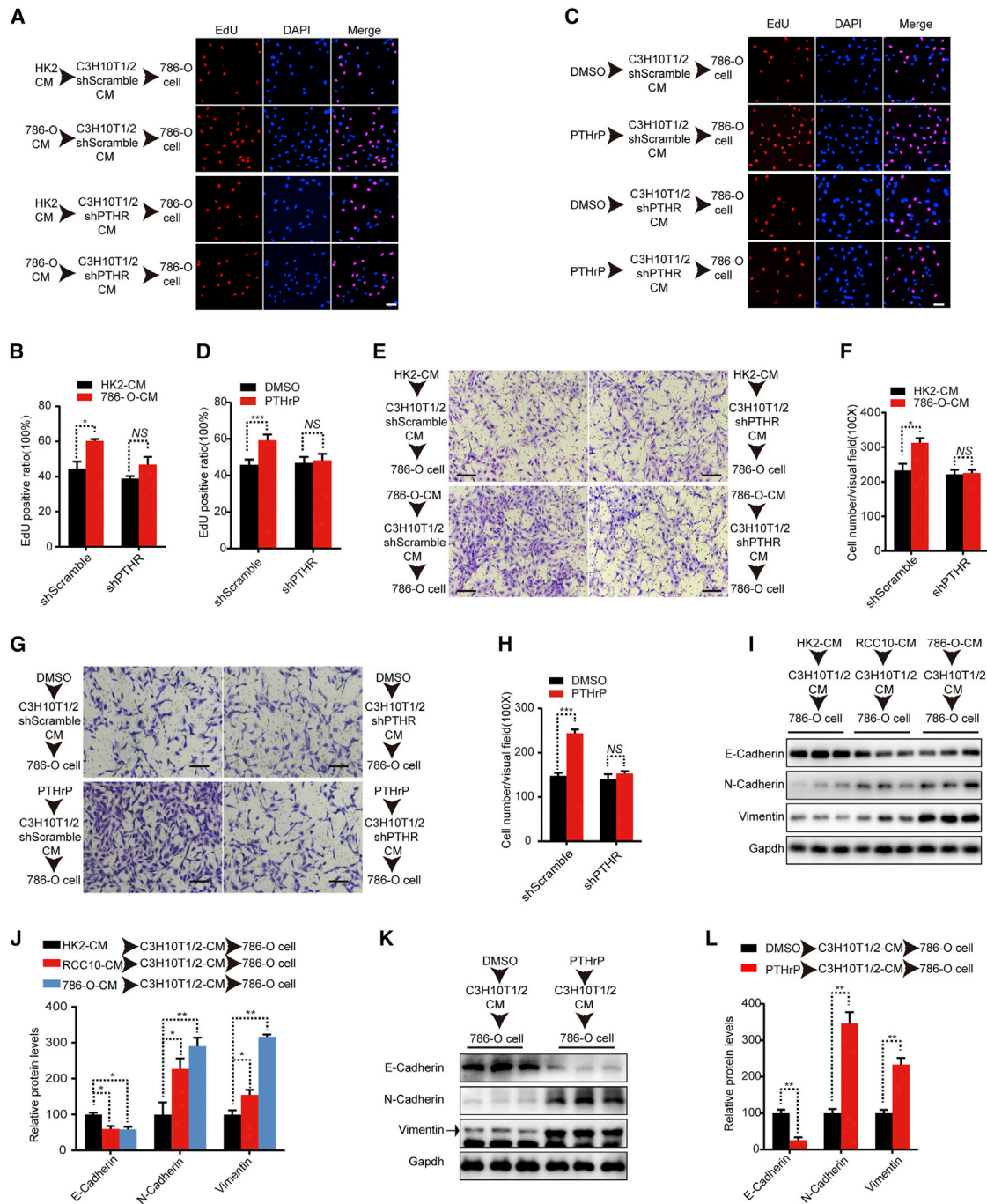
Figure 2. Communication between beige adipocytes and ccRCC cells promotes the proliferation and migration of 786-O cells

(A) Representative images showing EdU incorporation in 786-O cells treated with two-step CM as described in Figure S2A for 24 h (6 images per 3 biological replicates for each group). Scale bar, 50 μm.

(B) Ratio of EdU-positive 786-O cells in (A) (6 images per 3 biological replicates for each group).

(C) Representative images showing EdU incorporation in 786-O cells treated with two-step CM for 24 h (6 images per 3 biological replicates for each group). Scale bar, 50 μm.

(D) Ratio of EdU-positive 786-O cells in (C) (6 images per 3 biological replicates for each group).

(E) Representative images of 786-O cells that cultured in *trans*-well plates and treated with two-step CM as described in Figure S2A (6 images per 3 biological replicates for each group). Scale bar, 100 μm.

(F) Quantification of the average number of migrating 786-O cells in (E) (6 images per 3 biological replicates for each group).

(G) Representative images of 786-O cells that cultured in trans-well plates and treated with two-step CM (6 images per 3 biological replicates for each group). Scale bar, 100 μm.

(legend continued on next page)

mitochondrial proteins (Figures 1F and S1M). Notably, RCC10 and 786-O cell media also upregulated the mRNA and protein levels of thermogenic and mitochondrial genes in primary brown adipocytes (Figures S1N and S1O). These results indicated that secretory products or metabolites of ccRCC cells modulated the browning of adipocytes in tumor-adjacent PAT.

Based upon previous reports, several other tumor-secreted cytokines might activate white adipocyte browning, including PTHrP, zinc-alpha-2-glycoprotein-1 (AZGP1), growth/differentiation factor 15 (GDF15), and interleukin-6 (IL6) (Huang et al., 2016). We compared the expression of these cytokines in ccRCC and normal kidney tissues from the Cancer Genome Atlas (TCGA) website (https://www.cbioportal.org/) but only identified an increase in *PTHLH* mRNA (encoding PTHrP) in renal tumors versus normal tissue (Figures S1P–S1S). In addition, by analysis of the TCGA dataset, we revealed a positive correlation between *PTHLH* expressions and tumor grades, as well as a significant inverse correlation between *PTHLH* expressions and survival rates of individuals with ccRCC (p = 0.0035) (Figures 1G and 1H).

Consistent with the TCGA data, we found that *PTHLH* mRNA levels in ccRCC cells and PTHrP protein concentration in their culture media were higher than those in HK2 cells or the media, respectively (Figures 1I and S1T). We also revealed that *PTHLH* mRNA abundance was higher in ccRCCs than that in normal paracarcinoma tissue (Figure 1J) and that serum PTHrP concentration was also higher in individuals with ccRCC (Figure S1U). To validate the functional significance of elevated PTHrP expression in ccRCC tumors, we treated mature white adipocytes with recombinant PTHrP and it was sufficient to upregulate adipocyte browning in a dose-dependent manner, as indicated by increased UCP1 protein expression (Figures 1K and S1V).

Neutralizing PTHrP in ccRCC cell CM with a specific anti-PTHrP antibody abrogated the upregulation of UCP1 in the medium-treated adipocytes (Figure 1L). Likewise, silencing PTHrP's cell surface receptor (PTHR) in C3H10T1/2-derived adipocytes efficiently impaired the upregulation of UCP1 caused by treatment with ccRCC cell CM (Figures 1M and S1W). Moreover, MitoTracker staining also showed higher fluorescence intensity in PTHrP-treated adipocytes than in vehicle-incubated cells (Figure S1X). Consistently, treatment with media from 786-O or RCC10 cells elevated the phosphorylation of various endogenous PKA substrates, as well as HSL and CREB, both of which are well-known direct PKA substrates (Figure 1N). Recombinant PTHrP phenocopied the ccRCC CM-mediated browning effects (Figure S1Y). In line with this, the PKA inhibitor H89 or KT5720 efficiently suppressed the ccRCC CM- or PTHrP-mediated increase in UCP1 protein levels and PKA substrate phosphorylation (Figures 1N and S1Y). Finally, we found that either ccRCC CM or PTHrP could markedly elevate the basal, uncoupled,

and maximal oxygen consumption rate (OCR) in adipocytes (Figures 1O–1R).

Beige adipocytes promote ccRCC cell proliferation and migration

Given their proximity to tumors, we questioned whether browning of tumor-adjacent adipocytes facilitates ccRCC progression. To mimic putative bi-directional communication between ccRCCs and adipocytes, we designed a series of parallel two-stage CM treatment experiments with PTHR-silenced C3H10T1/2 cells (shPTHR) and control cells (shScramble) (Figure S2A). In detail, we pre-treated shScramble or shPTHR adipocytes with CM (from non-tumor cells or ccRCCs) or PTHrP to promote their browning. The adipocyte CM were applied to fresh cultures of 786-O or RCC10 cells (Figure S2A). Incorporation of 5-ethynyl-2′-deoxyuridine (EdU) showed that CM from beige adipocytes pre-treated with ccRCC CM or PTHrP promoted cell proliferation in the recipient ccRCCs, whereas CM from adipocytes pre-treated with HK2-CM or DMSO had little effects on the proliferation of ccRCCs (Figures 2A–2D, S2B, and S2C).

Given shPTHR adipocytes cannot be induced into beige cells (Figure 1M), we tested how CM from shPTHR adipocytes affected ccRCC growth. In contrast to medium from shScramble adipocytes, medium conditioned by shPTHR adipocytes had little effect to promote EdU incorporation in 786-O or RCC10 cells, regardless of whether the shPTHR adipocytes were pre-treated with ccRCC CM or PTHrP (Figures 2A–2D and S2B–S2G). Consistently, a trans-well assay showed that two-step CM collected from shScramble adipocytes promoted the migration of ccRCC cells, whereas co-culture with the two-step CM from shPTHR adipocytes did not (Figures 2E–2H and S2H–S2M). In support of this finding, immunoblotting showed that 786-O cells treated with CM from beige adipocytes had reduced abundance of epithelial marker E-cadherin and elevated abundance of mesenchymal markers N-cadherin and vimentin (Figures 2I–2L), suggesting that factors in CM from beige adipocytes potentiate a phenotypic change toward an epithelial-mesenchymal transition (EMT) in ccRCCs. We conclude that, within the ccRCC TME, the adjacent adipocytes that have undergone browning are endowed with the ability to enhance ccRCC proliferation and migration via feedback communication.

Crosstalk between ccRCCs and adipocytes promotes renal tumor growth in xenografted mice

To validate the effects of communication between ccRCC cells and adipocytes *in vivo*, ccRCC xenografts were generated with these two cell types. Initially, we injected the 786-O: C3H10T1/2 cell mixture at a 3:1 ratio into the right side of B-NDG immunodeficient mice, and the same total number of 786-O cells into each mouse's left side (Figures S3A and S3B). Strikingly, the

---

(H) Quantification of the average number of migrating 786-O cells in (G) (6 images per 3 biological replicates for each group).

(I) Immunoblots of E-cadherin, N-cadherin, and vimentin in 786-O cells after exposure to two-step CM for 24 h (n = 3; representative of 3 biological replicates for each group).

(J) Analysis of protein abundance of E-cadherin, N-cadherin, and vimentin in (I) (1 technical replicate of 3 biological replicates for each group).

(K) Immunoblots of E-cadherin, N-cadherin, and vimentin in 786-O cells after exposure to two-step CM for 24 h. Arrow indicates the vimentin protein band (n = 3; representative of 3 biological replicates for each group).

(L) Analysis of protein abundance of E-cadherin, N-cadherin, and vimentin in (K) (1 technical replicate of 3 biological replicates for each group).

Data were expressed as means ± SEM. *p < 0.05, **p < 0.01, ***p < 0.001 by unpaired two-tailed Student's t tests (B, D, F, H, J, and L).
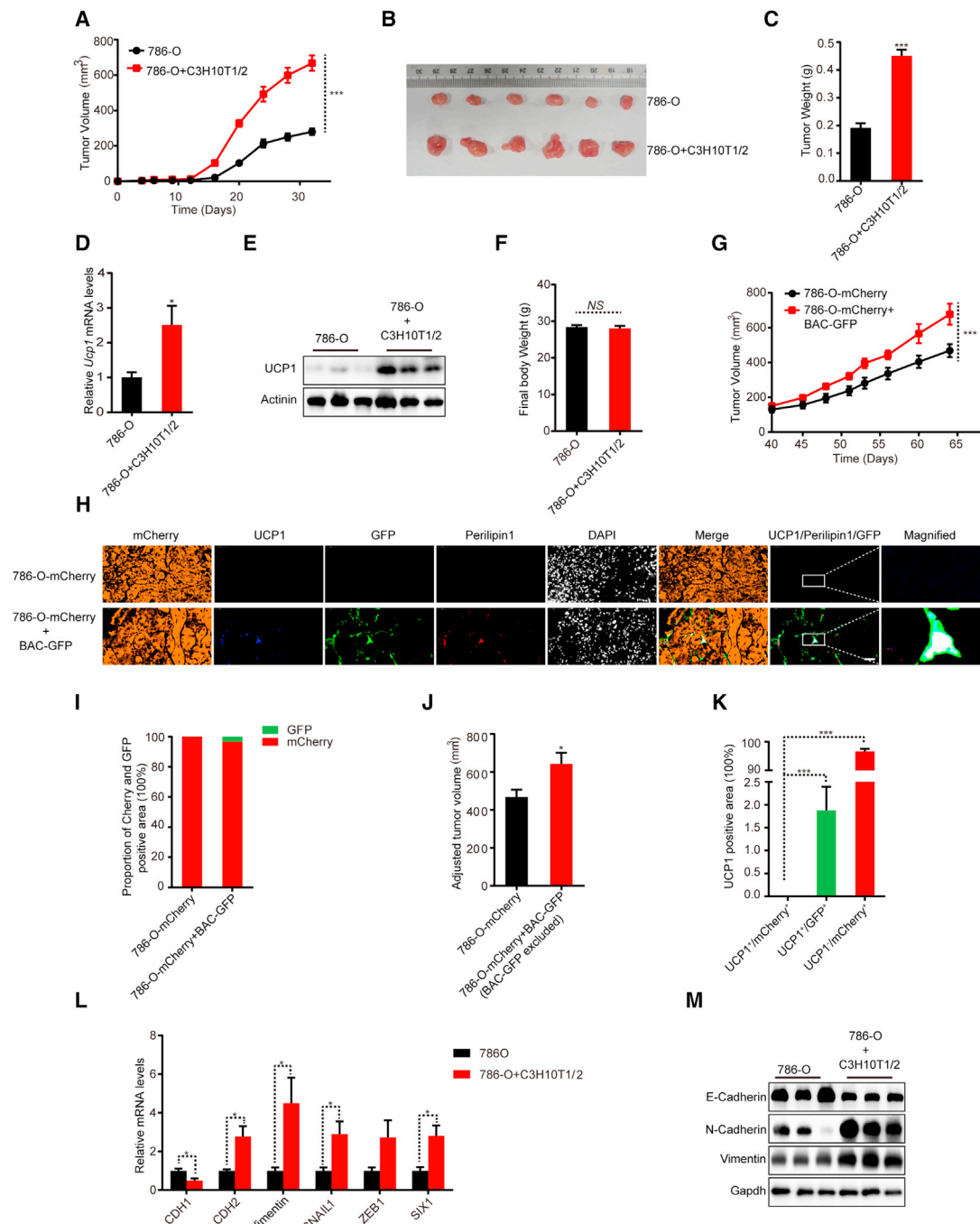
Figure 3. Adipocyte browning promotes ccRCC tumor progression in xenografts

(A) A subcutaneous tumor growth curve from 786-O cells (1×10^6 cells per mouse) or 786-O cells (1×10^6 cells per mouse) mixed with C3H10T1/2 cells (0.25×10^6 cells per mouse) (n = 6 mice per group).

(B) Representative images of xenografts in (A) at day 32 (n = 6 mice per group).

(C) Weights of xenograft tumors in (B) at day 32 (n = 6 mice per group).

(D) Mouse *Ucp1* mRNA expression in xenograft tumors derived from (B) (1 technical replicate of 6 biological replicates per group).

(E) Immunoblots of UCP1 in xenograft tumors derived from (B) (n = 3; representative of 3 biological replicates per group).

(F) Body weights of mice monitored in (A) at day 32 (n = 6 mice per group).

(G) A subcutaneous tumor growth curve from 786-O-mCherry cells (1×10^6 cells per mouse) or 786-O-mCherry cells (1×10^6 cells per mouse) mixed with BAC-GFP cells (0.25×10^6 cells per mouse) (n = 6 mice per group).

(H) Representative mIHC images of xenograft tumors in (G) at day 65 (9 images per 3 biological replicates per group). Orange, mCherry; blue, UCP1; green, GFP; red, Perilipin1; gray, DAPI. Scale bar, 50 μm.

(legend continued on next page)

786-O + C3H10T1/2 cell mixture generated huge xenograft tumors, and the mice quickly died (Figure S3C).

To overcome the problem of early lethality in the xenografted mice, we adjusted the 786-O: C3H10T1/2 cell ratio to 4:1 in the mixture. On the other hand, to avoid the potential interaction between two tumors in bilateral injection, we injected the mixed cells in one group of B-NDG mice, and the 786-O-only- or C3H10T1/2-only-injected mice were used as controls (Figures 3A and S3D). Although C3H10T1/2-cell-only injection did not produce detectable xenograft tumors or other lumps throughout the experiments (Figure S3D, dotted circles), other injections produced measurable tumors within 16 days (Figure 3A). We continuous monitored the tumor growth and revealed that the growth rate of tumors containing 786-O and C3H10T1/2 cells was higher than that of tumors originated from 786-O cells alone (Figure 3A). Consistently, tumors that originated from mixed ccRCC and adipocyte cells (786-O + C3H10T1/2 cells) were larger and heavier than control (786-O) tumors at 32 days after injection (Figures 3B and 3C). As evidence for the browning of co-injected C3H10T1/2 cells, Ucp1 mRNA and protein were upregulated in the tumors of mixed 786-O + C3H10T1/2 cell origin (Figures 3D and 3E). We did not detect any obvious difference in body weight or carcass body weight between 786-O + C3H10T1/2 mice and 786-O mice, indicating that cachexia was not obvious during the assays (Figures 3F and S3E).

To further track the proliferation of ccRCCs and adipocytes within the xenografts, we constructed a subcell line of 786-O labeled with mCherry (786-O-mCherry) and a mouse brown/beige pre-adipocyte cell line (BAC) labeled with GFP (BAC-GFP). BAC has similar browning potential, compared with pre-adipocytes isolated from brown adipose tissue (BAT) (Figures S3F and S3G), and BAC-only injection did not produce detectable tumors throughout the observation period (Figure S3H). Consistent with our results using non-labeled cells, the growth rate of ccRCCs containing BAC-GFP was robustly higher than that of control tumors only containing 786-O-mCherry cells (Figures 3G and S3I). Multiplex IHC (mIHC) staining demonstrated that both red (786-O-mCherry) and green (BAC-GFP) fluorescence could be detected in tumors of mixed-cell origin (Figure 3H, bottom row of images). The proportion of GFP-positive area in mixed-cell tumor sections averaged just 3.3%, while that of mCherry-positive area was 96.7% (Figure 3I). Next, we used the proportion of mCherry-positive area measured in each tumor to calculate the tumor volume occupied by 786-O cells alone, which showed that the ccRCC cell (786-O)-occupied volume in mixed-cell tumors was markedly greater than that in control tumors (Figure 3J).

Because UCP1 abundance was upregulated in mixed-cell xenograft tumors (Figure 3E), we investigated the extent to which the co-injected adipocytes versus ccRCC cells contributed to the phenotype. We performed immunofluorescence staining with tumor sections and did not detect any UCP1 signal in con-

trol tumors (Figure 3H, top row); whereas the UCP1 in mixed-cell tumors colocalized with Perilipin1 as well as with BAC-GFP (adipocyte tracer) (Figure 3H, bottom right). We normalized the UCP1-positive area by underlying mCherry- or GFP-positive area over entire sections and further substantiated that elevated UCP1 abundance found in mixed-cell tumors was due to expression of UCP1 in the co-injected adipocytes (Figures 3I and 3K).

Next, we detected the downregulation of CDH1 and the upregulation of genes such as CDH2, vimentin, SNAIL1, ZEB1, and SIX1 in mixed-cell tumors relative to control tumors (Figure 3L). Immunoblotting of tumor lysates verified the upregulation of N-cadherin and vimentin, and the downregulation of E-cadherin in mixed-cell tumors (Figure 3M). These results suggest that co-injection of adipocytes may induce an EMT program in mixed-cell ccRCCs.

Inhibition of adipocyte browning blocks adipocyte-promoted ccRCC proliferation and tumor growth

Given that suppressing adipocyte browning abrogated adipocyte-mediated ccRCC cell proliferation and migration (Figures 2A–2H and S2B–S2M), we next sought to determine whether inhibition of adipocyte browning could constrain ccRCC growth in vivo. To this end, we generated two adipocyte cell lines with impaired browning and/or uncoupled oxidative capacity—Pgc1α knockdown BAC (BAC-shPgc1α) and Ucp1 knockdown BAC (BAC-shUcp1)—as well as BAC-Scramble as a control (Figures S3J–S3M). These adipocyte cells were co-injected with 786-O ccRCC cells into B-NDG mice. The tumor volume of ccRCCs containing BAC-Scramble was higher than that of control (786-O) tumors (Figure 4A). In contrast, Pgc1α or Ucp1 depletion in BAC markedly impaired the ability of adipocytes to promote tumor growth (Figure 4A). Whereas tumors containing BAC-Scramble were larger and heavier than control tumors, those containing shPgc1α- or shUcp1 were not (Figures 4B and 4C). Thus, genetic inhibition of browning (shPgc1α), or simply of uncoupled respiration (shUcp1) in BAC was sufficient to eliminate their contribution to tumor growth. mIHC staining of tumor sections revealed greater expression of Ki67 (a proliferation marker) in tumors containing co-injected BAC-Scramble, relative to control tumors (786-O alone) (Figures 4D and 4E). We found that the higher Ki67 expression colocalized with the ccRCC cell marker paired box 8 (PAX8) (Figure 4F); whereas silencing Pgc1α or Ucp1 in co-injected BAC resulted in Ki67 staining more comparable with that of 786-O along (Figures 4D and 4E). qRT-PCR, immunofluorescence staining, and immunoblotting of tumor cells all indicated that adipocyte-promoted upregulation of UCP1 levels was suppressed in tumors associated with co-injected BAC-shPgc1α or BAC-shUcp1 (Figures 4G–4I). As a critical control, mIHC staining further excludes the possibility that UCP1 in 786-O + BAC-Scramble tumors originated from PAX8-labeled ccRCC cells (Figure 4H). We also detected a phenotypic change toward an EMT in 786-O + BAC-Scramble

---

(I) Proportions (%) of mCherry-positive 786-O cells and GFP-positive BAC cells in (H) (9 images per 3 biological replicates for each group).

(J) Adjusted individual tumor volumes in (G) (n = 6 mice per group).

(K) Ratio of UCP1-positive BAC cells in (H) (9 images per 3 biological replicates for each group).

(L) Expression levels of EMT-related genes in xenograft tumors derived from (B) (1 technical replicate of 5 biological replicates per group).

(M) Immunoblots of E-cadherin, N-cadherin, and vimentin in xenograft tumor derived from (B) (n = 3; representative of 3 biological replicates per group).

Data were expressed as means ± SEM. *p < 0.05, **p < 0.01, ***p < 0.001 by two-way ANOVA (A and G) or unpaired two-tailed Student's t tests (C, D, F, and I–L).
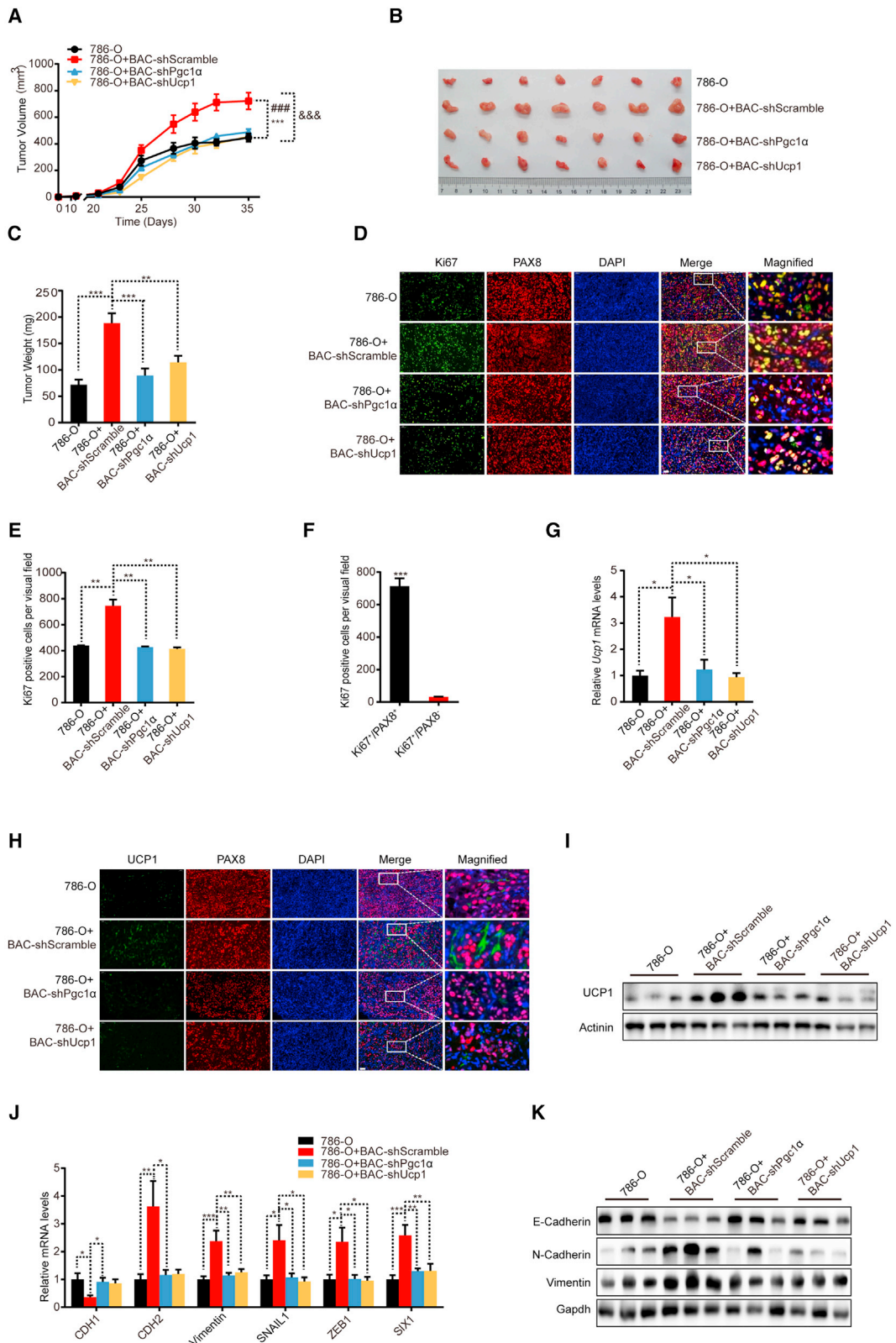
(legend on next page)

tumors, which was suppressed in tumors containing co-injected BAC-shPgc1α or BAC-shUcp1 (Figures 4J and 4K).

To avoid the off-target effects of shRNA-mediated knockdown, we constructed *Pgc1α* knockout BAC (BAC-Pgc1α-KO) and *Ucp1* knockout BAC (BAC-Ucp1-KO) using the CRISPR-Cas9 technique (Figures S3N and S3O). Consistent with the above observation, Pgc1α or Ucp1 ablation in BAC impaired the pro-tumorigenic effect of adipocytes (Figures S3P–S3R).

PTHrP-PTHR-PKA signaling promotes ccRCC cell proliferation, invasion, and metastasis

To elucidate the role of PTHrP-PTHR-PKA signaling in the crosstalk between ccRCC cells and adipocytes, we constructed PTHR knockout BAC (BAC-PTHR-KO), PKA knockout BAC (catalytic subunits of PKA ablated, BAC-PKA-KO), and PTHrP knockout 786-O cells (786-O-PTHLH-KO) (Figures S4A–S4C). We injected the 786-O cells with or without these genetically modified adipocytes into nude mice to generate xenograft tumors. The tumors containing BAC-Scramble displayed a strikingly higher growth rate than control (786-O only) tumors (Figures 5A–5C). By contrast, PTHR or PKA ablation in BAC impaired the tumor-promoting effect of adipocytes on renal tumor growth (Figures 5A–5C). Knockout of *PTHLH* in 786-O cells also suppressed the effect of BAC on promoting ccRCC growth (Figures 5A and 5B). Measurement of tumor weight supported these results (Figure 5C).

To further determine whether inhibition of adipocyte browning affects ccRCC cell lung metastasis *in vivo*, we performed a lung colonization assay with BAC-PTHR-KO and luciferase labeled 786-O cells (786-O-Luc). To mimic potential crosstalk between ccRCC cells and adipocytes, we pre-treated 786-O-Luc cells with medium from BAC-Scramble and BAC-PTHR-KO for 2 weeks (Figure S4D), and the 786-O-Luc cells were divided into three groups as follows: group 1, DMSO▶BAC-Scramble▶786-O-Luc; group 2, PTHrP▶BAC-Scramble▶786-O-Luc; and group 3, PTHrP▶BAC-PTHR-KO▶786-O-Luc. After 2-week treatment, E-cadherin levels were reduced, and N-cadherin and vimentin levels were upregulated in 786-O cells of group 2, but not in cells of groups 1 and 3 (Figure 5D). We then injected the treated 786-O cells into nude mice via the tail vein. Eight weeks after injection, whole-body bioluminescence (BL) imaging detected overt metastases in

the lungs of group 2 mice compared with groups 1 and 3 mice (Figures 5E and S4E); BL imaging and H&E staining of the segmented lungs further revealed that signals and number of metastatic lesions (arrows) were remarkably higher in the lungs of group 2 mice than in those of groups 1 and 3 (Figures 5F–5H).

According to previous reports, ccRCC invasion into PAT predicts poor prognosis (Bedke et al., 2009). Herein, we harvested clinical samples containing ccRCC tumors and the adherent fat tissue infiltrated by the tumor (Figures S4F and S4G). mIHC analysis showed that UCP1 signal overlapped with that of Perilipin1, but not with PAX8 (a ccRCC marker) (Figure S4H).

To better mimic the pathological setting of the PAT invasion and lung metastasis of ccRCC, we investigated the pro-tumor effect of adjacent beige adipocytes via an orthotopic kidney tumor model. 786-O-PTHLH-KO-Luc cells, 786-O-Scramble-Luc cells, or 786-O-Luc cells were orthotopically injected into the nude mice. Six weeks after injection, whole-body BL imaging revealed overt signals in the kidneys of mice injected with 786-O-Luc and 786-O-Scramble-Luc cells (Figures 5I and S4I); by contrast, mice injected with 786-O-PTHLH-KO-Luc cells showed markedly weaker BL signals than the other two control groups (Figures 5I and S4I).

To evaluate tumor invasion into PAT and the browning transformation of the adjacent PAT, we harvested the orthotopic xenograft tumors together with the PAT and performed mIHC analysis (Figure S4J). The presence of ccRCC cells in the adherent PAT indicated the invasion of orthotopic tumors into PAT (Figure S4J). With mIHC analysis of the tumor-PAT interface, we detected obvious UCP1 signals in the 786-O-Luc or 786-O-Scramble-Luc groups, which colocalized with Perilipin1 (Figure S4J). By contrast, in mice injected with 786-O-PTHLH-KO-Luc cells, the invasion of ccRCC tumor cells into adipose tissue was lower, and the browning features of adherent PAT were suppressed (Figure S4J). These data indicate that PTHrP (encoded by *PTHLH*) secreted from ccRCC confers a brown-like phenotype to PAT, which in turn promotes ccRCC growth and invasion.

Obvious BL signals in the resected lungs of mice injected with 786-O-Luc or 786-O-Scramble-Luc cells indicated overt lung metastases of these ccRCC tumors (Figure 5J). However, PTHrP deletion blocked lung metastases of 786-O cells (Figure 5J). In line with this, H&E staining showed considerably fewer nodules

---

Figure 4. Inhibition of adipocyte browning blocks adipocyte-promoted ccRCC cell proliferation and tumor growth

(A) A subcutaneous tumor growth curve from 786-O cells (1×10^6 cells per mouse) or 786-O cells (1×10^6 cells per mouse) mixed with respective BAC cells (0.25×10^6 cells per mouse) (n = 7 mice per group). ***$p < 0.001$ in 786-O + BAC-shPgc1α versus 786-O + BAC-shScramble, ###$p < 0.001$ in 786-O + BAC-shUcp1 versus 786-O + BAC-shScramble, &&&$p < 0.001$ in 786-O versus 786-O + BAC-shScramble.

(B) Representative images of xenografts in (A) at day 35 (n = 7 mice per group).

(C) Weights of xenograft tumors in (B) at day 35 (n = 7 mice per group).

(D) Representative mIHC images of xenograft tumors in (B) (6 images per 3 biological replicates for each group). Green, Ki67; red, PAX8; blue, DAPI; yellow, Ki67+/PAX8+ cells in merged image. Scale bar, 50 μm.

(E) Quantification of the average number of Ki67-positive cells in (D) (6 images per 3 biological replicates for each group).

(F) Quantification of the average number of Ki67-positive 786-O cells (PAX8-positive cells) in (D) (6 images per 3 biological replicates for each group).

(G) Mouse *Ucp1* mRNA expression in xenograft tumors derived from (B) (1 technical replicate of 6 biological replicates per group).

(H) Representative mIHC images of xenograft tumors in (B) (6 images per 3 biological replicates in total). Green, UCP1; red, PAX8; blue, DAPI. Scale bar, 50 μm.

(I) Immunoblots of UCP1 in xenograft tumors derived from (B) (n = 3; representative of 3 biological replicates per group).

(J) Expression levels of EMT-related genes in xenograft tumors derived from (B) (1 technical replicate of 6 biological replicates per group).

(K) Immunoblots of E-cadherin, N-cadherin and vimentin in xenograft tumors derived from (B) (n = 3; representative of 3 biological replicates per group).

Data were expressed as means ± SEM. *$p < 0.05$, **$p < 0.01$, ***$p < 0.001$ by two-way ANOVA (A), one-way ANOVA (C, E, G, and J), or unpaired two-tailed Student's t tests (F).
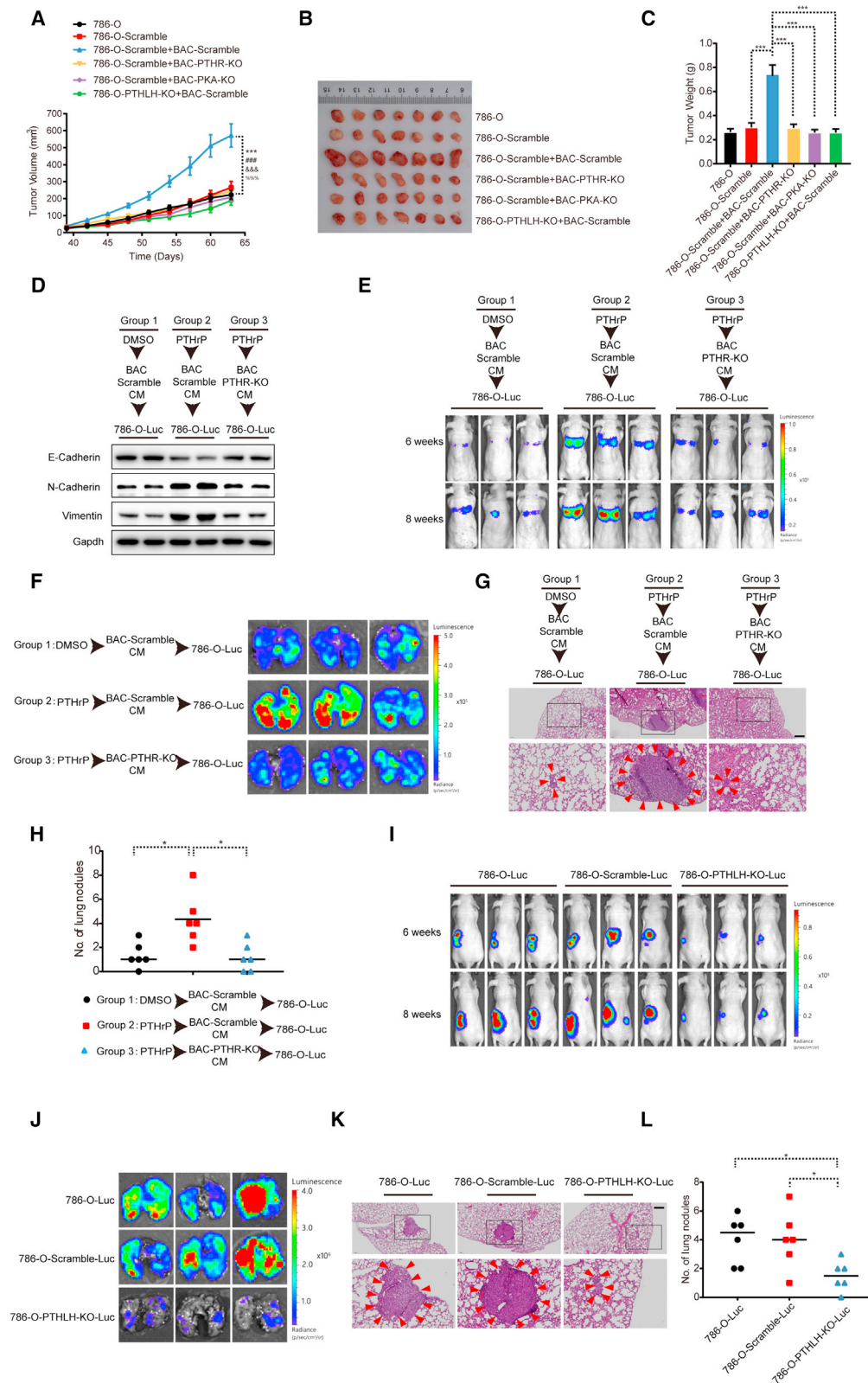
Figure 5. PTHLH-PTHR-PKA signaling promotes ccRCC cell proliferation and metastasis *in vivo*

(A) A subcutaneous tumor growth curve from 786-O cells (1 × 10⁶ cells per mouse) or 786-O cells (1 × 10⁶ cells per mouse) mixed with respective BAC cells (0.25 × 10⁶ cells per mouse) (n = 7 mice per group). ***p < 0.001 in 786-O-Scramble versus 786-O-Scramble + BAC-Scramble, ###p < 0.001 in 786-O-Scramble +

(legend continued on next page)

in the lungs of mice injected with 786-O-PTHLH-KO-Luc than in the other two groups (Figures 5K and 5L).

Small molecules released from adipocytes enhance the proliferation and migration of ccRCCs

Next, we sought to ascertain the mechanism by which perinephric beige adipocytes promote ccRCC tumor development. Beige adipocytes secrete numerous proteins and small molecules, such as metabolites, that might favorably alter the TME. Thus, we boiled CM from PTHrP- or ccRCC-CM-induced beige adipocytes (Figures 6A and S5A) and then removed denatured proteins by filtration, before incubating fresh 786-O ccRCC cells with the beige adipocyte CM. Interestingly, boiled and filtered adipocyte CM retained its ability to enhance the proliferation and migration of 786-O cells, comparable with non-boiled adipocyte CM (Normal CM) (Figures 6A–6D and S5A–S5D).

Considering that those small molecules, if not volatile, are probably more stable at high temperature than secreted proteins, we hypothesized that micromolecular metabolites left in boiled CM played a primary role in promoting ccRCC cell growth. Others have reported that adipocytes can feed free fatty acids (FFAs) to tumor cells (Nieman et al., 2011; Wang et al., 2017). Consistent with this, adipocytes incubated in ccRCC CM and treated with PTHrP secreted more FFAs than control cells (Figures S5E–S5H). By contrast, ccRCC CM- or PTHrP-induced FFA release from adipocytes was inhibited by H89 or silencing Pgc1α, Ucp1, or PTHR (Figures S5E–S5H). We detected increased phosphorylated HSL level in ccRCC CM- or PTHrP-treated adipocytes, and also found that H89 (or KT5720) treatment or knockdown of Pgc1α or Ucp1 completely abolished the increased phosphorylation of HSL (Figures 1N, S1Y, S5I, and S5J). These results validate the notion that lipolytic activity in adipocytes is enhanced during the PTHrP- or ccRCC CM-mediated browning process.

FFAs and glycerol are not the main fuel sources for ccRCC cell growth

Compatible with the increased FFA secretion from beige adipocytes in the TME, both RCC10 and 786-O cells exhibited higher expression of FFA transporters than HK2 cells (Figure S5K). However, the expression of genes involved in FFA oxidation (FAO) was lower in ccRCC cells than in HK2 cells (Figure S5L).

The OCR of HK2 cells was remarkably suppressed by Etomoxir (Eto, a CPT1α inhibitor) (Figure S5M), which inhibits the transport of FFAs into mitochondria (Wettersten et al., 2015), but not that of 786-O and RCC10 cells (Figures S5M and S5N). Thus, we inferred that catabolism of FFAs may be reduced in ccRCC versus non-tumor cells. Consistent with previous reports (Ackerman et al., 2018; Qiu et al., 2015), with H&E and Oil Red O staining, we detected gigantic lipid droplets within the cytoplasm of ccRCC tumor cells (Figure S5O).

To test whether deletion of CD36 abolishes the ccRCC proliferative advantage obtained from metabolite(s) secreted by adipocytes, we treated CD36 knockout 786-O cells (CD36-KO) with beige adipocyte CM (Figure S5P) and found that CD36 deletion had little effect on the proliferation and migration of cancer cells (Figures S5Q–S5T). These results support the notion that ccRCC cells preferentially transform FFAs to neutral triglycerides, rather than using FAO as a main fuel source, which is distinct from some other types of cancer (Iwamoto et al., 2018; Wen et al., 2017).

Glycerol is also produced and secreted during the lipolysis of beige adipocytes. We found that adipocytes exposed to ccRCC cell CM or PTHrP released more glycerol than control adipocytes, whereas H89 treatment or knockdown of PTHR, Pgc1α, or Ucp1 completely inhibited glycerol secretion from adipocytes (Figures S6A–S6D). EdU staining and trans-well assays showed no differences in proliferation and migration between the 786-O cells treated with glycerol and vehicle (Figures S6E–S6H).

Lactate released from beige adipocytes promotes ccRCC cell proliferation and migration

Given the observation of downregulated FAO in ccRCC cells and tumors, we hypothesized that some other beige adipocyte-derived metabolite(s) might constitute the primary energy source fueling rapid ccRCC tumor growth. According to previous reports, beige adipocytes exhibit increased glycolysis and lactate release (Weir et al., 2018; Nguyen et al., 2020). Consistent with this, we found that BAT exhibited markedly higher lactate release than other WAT (Figure S6I), and PTHrP-induced beige cells also released more lactate than white adipocytes (Figures 6E and S6J), whereas ablation of Pgc1α or Ucp1 substantially suppressed PTHrP-caused lactate release in adipocytes (Figure S6J). In line with this, PTHrP increased the extracellular

---

BAC-Scramble versus 786-O-Scramble + BAC-PTHR-KO, &&&p < 0.001 in 786-O-Scramble + BAC-Scramble versus 786-O-Scramble + BAC-PKA-KO, %%% p < 0.001 in 786-O-Scramble + BAC-Scramble versus 786-O-Scramble + BAC-PTHLH-KO + BAC-Scramble.

(B) Representative images of xenograft tumors in (A) at day 63 (n = 7 mice per group).

(C) Weights of xenograft tumors in (B) at day 63 (n = 7 mice per group).

(D) Immunoblots of E-cadherin, N-cadherin, and vimentin in 786-O-Luc cells after treatment described in Figure S4D (n = 2; representative of 3 biological replicates per group).

(E) Representative BL images of xenograft tumors of 786-O-Luc cells (1 × 10^6 cells per mouse) described in Figure S4D (6 images per 6 biological replicates for each group).

(F) Representative BL images of lung tissues in (E) (6 images per 6 biological replicates for each group).

(G) Representative H&E staining of lung tissues in (E) (18 images per 6 biological replicates for each group). Scale bar, 400 μm.

(H) Quantification of the average number of lung metastatic lesions in (G) (18 images per 6 biological replicates for each group).

(I) Representative BL images of orthotopic xenografts of 786-O-Luc cells (2 × 10^6 cells per mouse), 786-O-Scramble-Luc cells (2 × 10^6 cells per mouse) or 786-O-PTHLH-KO-Luc cells (2 × 10^6 cells per mouse) (6 images per 6 biological replicates for each group).

(J) Representative BL images of lung tissues in (I) (6 images per 6 biological replicates for each group).

(K) Representative H&E staining of lung tissues in (I) (18 images per 6 biological replicates for each group). Scale bar, 400 μm.

(L) Quantification of the average number of lung metastatic lesions in (K) (18 images per 6 biological replicates for each group).

Data were expressed as means ± SEM. *p < 0.05, **p < 0.01, ***p < 0.001 by two-way ANOVA (A) or unpaired two-tailed Student's t tests (C, H, and L).
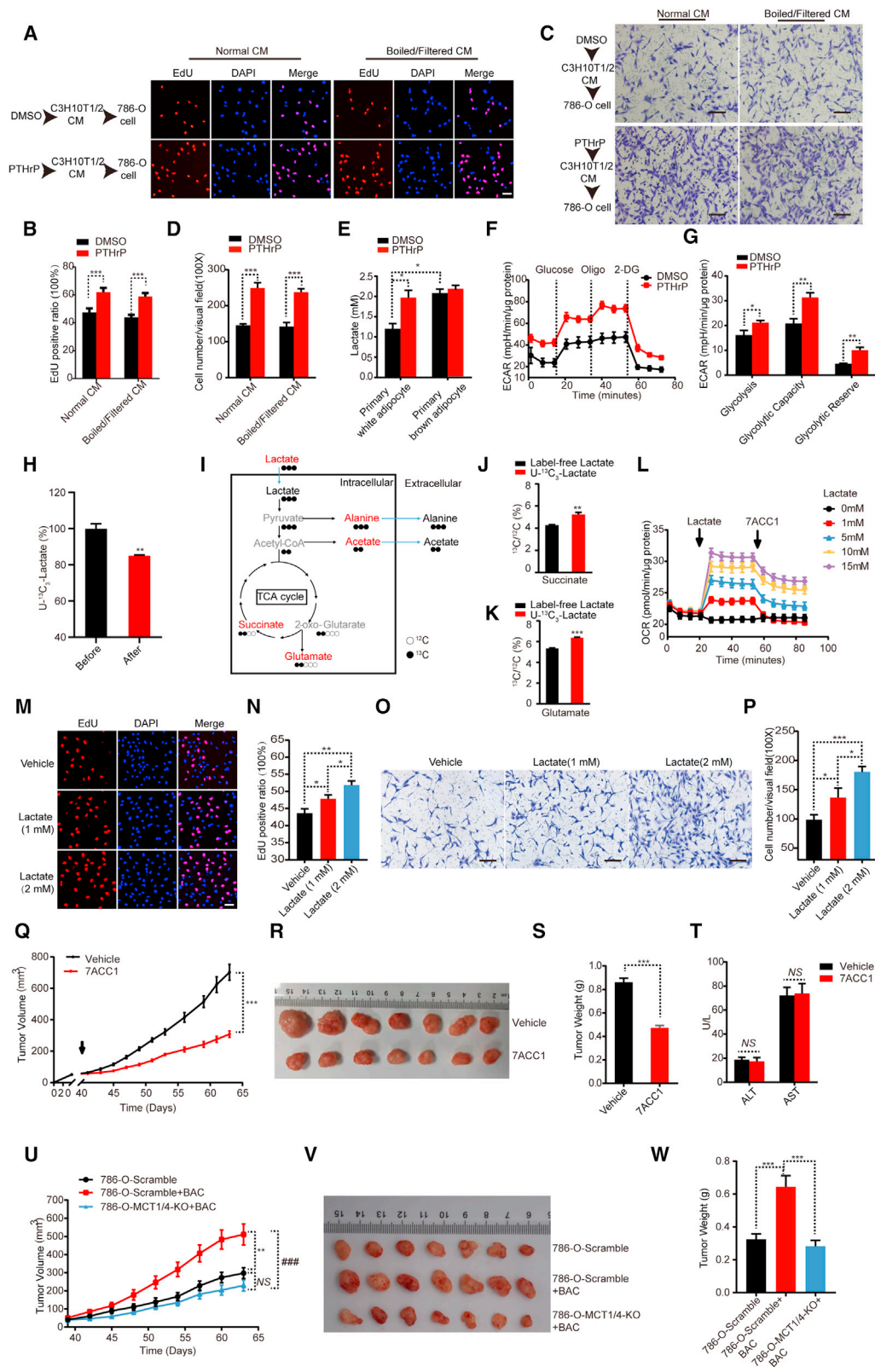
Figure 6. Lactate released from beige adipocytes promotes ccRCC cell proliferation and migration

(A) Representative images showing EdU incorporation in 786-O cells treated with two-step CM, as described in Figure S2A for 24 h, except that CM was boiled and filtered through a 0.2-μm filter before being applied to 786-O cells (6 images per 3 biological replicates for each group). Scale bar, 50 μm.

(legend continued on next page)

acidification rate (ECAR) of adipocytes (Figures 6F and 6G) and also elevated glycolytic proton efflux rate in adipocytes (Figures S6K and S6L), which validated the enhanced glycolysis of beige cells. Consistent with those findings, we found that the expression of genes that mediate lactate synthesis (LDHA) and transportation (MCT1 and MCT4) was considerably higher in ccRCC CM-induced beige adipocytes than in control adipocytes (Figure S6M).

Notably, the expressions of MCT1, MCT4, and LDHB were higher in RCC10 and 786-O cells than in HK2 cells (Figure S6N), suggesting increased uptake and usage of lactate in ccRCC cells. To further explore the mechanism of lactate utilization, we performed metabolic flux analysis in 786-O cells using [U-$^{13}C_3$]-labeled lactate as a tracer. The results of the NMR assay showed that 15.07% of total [U-$^{13}C_3$]-lactate in the culture medium was taken up by 786-O cells within 24 h (Figure 6H). In another metabolic flux analysis, we treated ccRCC cells with [U-$^{13}C_3$]-lactate or label-free lactate (control) (Figure 6I) and found that the amount of ^{13}C-succinate and ^{13}C-glutamate was higher in [U-$^{13}C_3$]-lactate-treated 786-O cells than in control cells (Figures 6I–6K). Moreover, the levels of ^{13}C-alanine and ^{13}C-acetate were markedly elevated in the medium of ccRCC cells pre-treated with [U-$^{13}C_3$]-lactate (Figures S6O and S6P). These results indicate that the lactate carbons are incorporated into intermediates and metabolites related to the TCA cycle. In line with this, lactate treatment led to a sharp increase in the OCR of 786-O cells, whereas inhibition of the cellular lactate transporters (MCT1/4) with a small molecule inhibitor (7ACC1)

caused a rapid reduction in the OCR of cancer cells (Figure 6L). Taken together, these results indicate that lactate serves as an important fuel incorporated into the TCA cycle of ccRCC cells.

We found that PTHrP increased the concentration of adipocyte-secreted lactate into the cell culture medium roughly by 2-fold in a short period (Figure 6E). Lactate treatment remarkably increased the proliferation and migration of 786-O cells (Figures 6M–6P). Next, in a similar CM transfer experiment, we added 7ACC1 into beige adipocyte CM before treating 786-O cells and revealed that 7ACC1 suppressed the enhancement of ccRCC cell proliferation and migration caused by beige adipocyte CM compared with the control group (Figures S6Q–S6X).

Inhibition of lactate importation into ccRCC cells impairs beige adipocyte-induced ccRCC tumor growth

Next, we treated xenograft tumor-bearing mice with 7ACC1 to investigate the role of lactate in beige adipocyte-induced tumor growth. 7ACC1 administration substantially suppressed tumor growth (Figure 6Q) and reduced the size and weight of tumors originated from mixed ccRCC cells and adipocytes (Figures 6R and 6S), without affecting the serum alanine transaminase (ALT) and aspartate aminotransferase (AST) levels (Figure 6T). We also constructed a lactate transporter knockout 786-O cell line (786-O-MCT1/4-KO) (Figure S6Y) and generated xenograft tumors with 786-O-MCT1/4-KO and BAC (Figure 6U). Consistently, MCT1/4 deletion in 786-O cells decreased growth rate and reduced the size and weight of the xenograft tumors (Figures 6U–6W).

(B) Ratio of EdU-positive 786-O cells in (A) (6 images per 3 biological replicates for each group).

(C) Representative images of 786-O cells that cultured in trans-well plates and treated with two-step CM as described in (A) (6 images per 3 biological replicates for each group). Scale bar, 100 μm.

(D) Quantification of the average number of migrating 786-O cells in (C) (6 images per 3 biological replicates for each group).

(E) Lactate released from primary white or brown adipocytes treated with vehicle or PTHrP (50 ng/mL) for 3 h (1 technical replicate of 8 biological replicates per group).

(F) The ECAR of differentiated C3H10T1/2 cells treated with vehicle or PTHrP (50 ng/mL) for 24 h (1 technical replicate of 5 biological replicates per group).

(G) Basal glycolysis, glycolytic capacity, and glycolytic reserve were determined in (F) (1 technical replicate of 5 biological replicates per group).

(H) The remaining levels of [U-$^{13}C_3$]-lactate in the cultured media of 786-O cells treated with 5 mM label-free lactate or [U-$^{13}C_3$]-lactate for 24 h (1 technical replicate of 3 biological replicates per group).

(I) Tracer scheme illustrating the flux of [U-$^{13}C_3$]-lactate into TCA cycles.

(J) ^{13}C enrichment of succinate in 786-O cells after treatment with [U-$^{13}C_3$]-lactate for 24 h (1 technical replicate of 3 biological replicates per group).

(K) ^{13}C enrichment of glutamate in 786-O cells after treatment with [U-$^{13}C_3$]-lactate for 24 h (1 technical replicate of 3 biological replicates per group).

(L) The OCR of 786-O cells treated with indicated concentrations of lactate following pH adjusted to 7.4 (1 technical replicate of 7 biological replicates per group). Lactate and 7ACC1 (10 μM) were injected at indicated time point, respectively.

(M) Representative images showing EdU incorporation in 786-O cells exposed to vehicle or lactate (1 mM or 2 mM) for 24 h (6 images per 3 biological replicates for each group). Scale bar, 50 μm.

(N) Ratio of EdU-positive 786-O cells in (M) (6 images per 3 biological replicates for each group).

(O) Representative images of 786-O cells that cultured in trans-well plates and treated with vehicle or lactate (1 or 2 mM) for 24 h (9 images per 3 biological replicates for each group). Scale bar, 100 μm.

(P) Quantification of the average number of migrating 786-O cells in (O) (9 images per 3 biological replicates for each group).

(Q) A subcutaneous tumor growth curve from 786-O cells (1 × 10⁶ cells per mouse) mixed with BAC cells (0.25 × 10⁶ cells per mouse) at indicated time points (n = 7 mice per group). The treatment with vehicle or 7ACC1 (3 mg/kg) began when volume of xenografts reached approximately 50 mm³. Arrow indicates initiation of drug treatment.

(R) Representative images of xenograft tumors in (Q) at day 63 (n = 7 mice per group).

(S) Weights of xenograft tumors in (R) at day 63 (n = 7 mice per group).

(T) Serum ALT and AST levels of mice in (Q) at day 63 (n = 7 in total).

(U) A subcutaneous tumor growth curve from 786-O-Scramble cells (1 × 10⁶ cells per mouse) or respective 786-O cells (1 × 10⁶ cells per mouse) mixed with BAC cells (0.25 × 10⁶ cells per mouse) (n = 7 mice per group). **p < 0.01 in 786-O-Scramble versus 786-O-Scramble + BAC, ###p < 0.001 in 786-O-MCT1/4-KO + BAC versus 786-O-Scramble + BAC; NS, p > 0.05 in 786-O-MCT1/4-KO + BAC versus 786-O-Scramble.

(V) Representative images of xenograft tumors in (U) at day 63 (n = 7 mice per group).

(W) Weights of xenograft tumors in (V) at day 63 (n = 7 mice per group).

Data were expressed as means ± SEM. *p < 0.05, **p < 0.01, ***p < 0.001 by unpaired two-tailed Student's t tests (B, D, E, G, H, J, K, S, and T), one-way ANOVA (N, P, and W), or two-way ANOVA (Q and U).

Our group and others found that white adipocytes release less lactate than beige adipocytes (Figures S7A–S7C) (Okamatsu-Ogura et al., 2020; Shamsi et al., 2020). Therefore, we compared the effects of the two types of adipocytes on ccRCC tumor growth *in vivo*. To this end, we differentiated two types of white adipocytes from 3T3L1 (3T3L1-white) and C3H10T1/2 (C3H10T1/2-white) cells, and two types of beige adipocytes from 3T3L1 (3T3L1-beige) and C3H10T1/2 (C3H10T1/2-beige) cells. Then, xenograft tumors were generated by injecting these adipocytes together with 786-O cells into nude mice. As expected, beige adipocytes (3T3L1-beige and C3H10T1/2-beige) markedly increased the growth rates of ccRCC tumors (Figure S7D), as well as tumor size and weight compared with white adipocytes (Figures S7E and S7F).

Inhibitors of adipocyte browning enhance TKI efficacy

Previously, the therapeutic efficacy of TKIs has been reported to be reduced in some cases, for reasons that remain unclear (Rini and Atkins, 2009). Relevant to this clinical issue—as well as to our findings that ccRCC tumor growth is stimulated by adjacent beige adipocytes—it has been shown that the TKIs sunitinib and axitinib promote adipocyte browning (Mao et al., 2017; Qiu et al., 2018). Consistent with those findings, we found that treating white adipocytes with four TKIs all substantially increased the expression of the browning markers *Ucp1*, *Pgc1α*, and *Dio₂* in white adipocytes (Figure 7A), further confirming that TKIs promote adipocyte browning. Treatment with TKIs also upregulated the expression of genes involved in lipolysis, including *Atgl* and *Hsl* in adipocytes (Figure 7B). Moreover, when we treated ccRCC cell lines (786-O or RCC10) with four different TKIs we found they all increased the expression of *PTHLH* (Figure 7C).

To assess the role of TKI-promoted adipocyte browning *in vivo*, we treated xenograft tumor-bearing mice with two PKA inhibitors, KT5720 and H89. As shown in Figures 7D–7F and S7G, sunitinib, H89 or KT5720 alone partially suppressed tumor growth relative to that in the vehicle group; while combination treatment (sunitinib + H89 or sunitinib + KT5720) substantially suppressed tumor growth compared with sunitinib alone. The combination of sunitinib + H89 or sunitinib + KT5720 markedly reduced tumor size and weight (Figures 7E, S7F and S7H). Notably, these drugs alone or in combination did not elevate serum ALT and AST levels (Figures 7G and S7I).

With the immunostaining analysis of tumor sections, we revealed that sunitinib treatment increased the abundance of UCP1 (Figures 7H and 7I). By contrast, in the groups receiving combination treatment, H89 or KT5720 substantially blocked sunitinib-elevated UCP1 levels in adipocytes (Figures 7H, S7I and S7J). The level of Ki67 in ccRCC cells was lower in combination treatment groups than in those receiving sunitinib alone (Figures 7J and 7K). qRT-PCR showed that combination treatment (sunitinib + H89 or sunitinib + KT5720) substantially increased transcription of *CDH1* and decreased mRNA levels of *CDH2*, *vimentin*, *ZEB1*, and *SIX1* (Figure 7L). Immunoblotting verified the upregulation of E-cadherin and the downregulation of N-cadherin and vimentin in the combination-treated tumors (Figures 7M, S7K, and S7L).

DISCUSSION

Perirenal fat infiltration during ccRCC tumor development is closely associated with an inferior survival rate. However, the detailed mechanism to explain this association remains elusive. In this study, we found that ccRCCs release PTHrP to promote PAT browning, which in turn results in the release of lactate into the TME, constituting a novel putative mechanism of enhanced ccRCC tumor growth. This phenomenon by which ccRCCs "feed" themselves by promoting the beiging of the adjacent PAT might explain why ccRCC tumors are prone to infiltrate fat tissue and why this phenomenon is associated with poorer prognosis. Interestingly, previous reports have documented non-cancerous cells in the TME are induced to "feed" the tumor (Goossens et al., 2019; Nieman et al., 2011; Maguire et al., 2021). For example, tumor-associated macrophages (TAMs) feed cholesterol to tumors to assist their growth, which in turn leads to reduce TAM activity, providing a more permissive environment for tumor growth (Goossens et al., 2019).

Lung-carcinoma-promoted WAT browning contributes to cachexia and leads to a wasting disorder of adipose tissue (Kir et al., 2014), whereas we found that the beige adipocytes in PAT secrete lactate that enhance ccRCC tumor growth, invasion, and metastasis. Consistently, other tumors promote and fully hijack the reprogramming of adjacent non-cancerous tissue (Chrysovergis et al., 2014; Elattar et al., 2018). For example, breast cancer cells promote the conversion of adjacent adipocytes into cancer-associated adipocytes (CAAs, characterized as the loss of adipocyte markers including FABP4), which in turn enhances the motility of cancer cells by secreting PAI-1 (Carter and Church, 2012). Conversely, we found that ccRCC cells increased uncoupled respiration in adjacent adipocytes without affecting FABP4 abundance, indicating that white adipocytes in PAT are transformed into beige adipocytes distinct from CAAs. The adipocytes of PAT are reported to have a higher propensity to convert to beige adipocyte compared with those in subcutaneous WAT (Jespersen et al., 2019; Wu et al., 2016). Here, we did not find the typical multilocular adipocytes of the BAT but instead detected a subset of adipocytes showing a paucilocular phenotype (a hallmark of WAT browning) in adjacent PAT (Brestoff and Artis, 2015). These findings suggest that the ccRCC-induced PAT browning might possess some unique features compared with browning of the visceral or subcutaneous fat. The primary function of the WAT is to store energy in the form of lipid droplets, and thus the catabolic activity in WAT is suppressed to a minimum level (Kiefer et al., 2012). Certain conditions (e.g., cold exposure or genetic mutations) stimulate browning of the WAT (Bartelt and Heeren, 2014). During WAT browning, catabolism inside beige adipocytes is markedly enhanced, leading to the superfluous production of lactate in excess of that consumed by beige adipocytes themselves (Okamatsu-Ogura et al., 2020; Tews et al., 2019). Therefore, compared with white adipocytes, beige adipocytes secrete more lactate into the extracellular environment, which could be utilized by adjacent cancer cells.

We found that genetic and pharmacological inhibition of adipocyte browning blocked the bi-directional communication between ccRCC cells and adjacent adipocytes, suppressing ccRCC progression. Reasonably, one mechanism by which
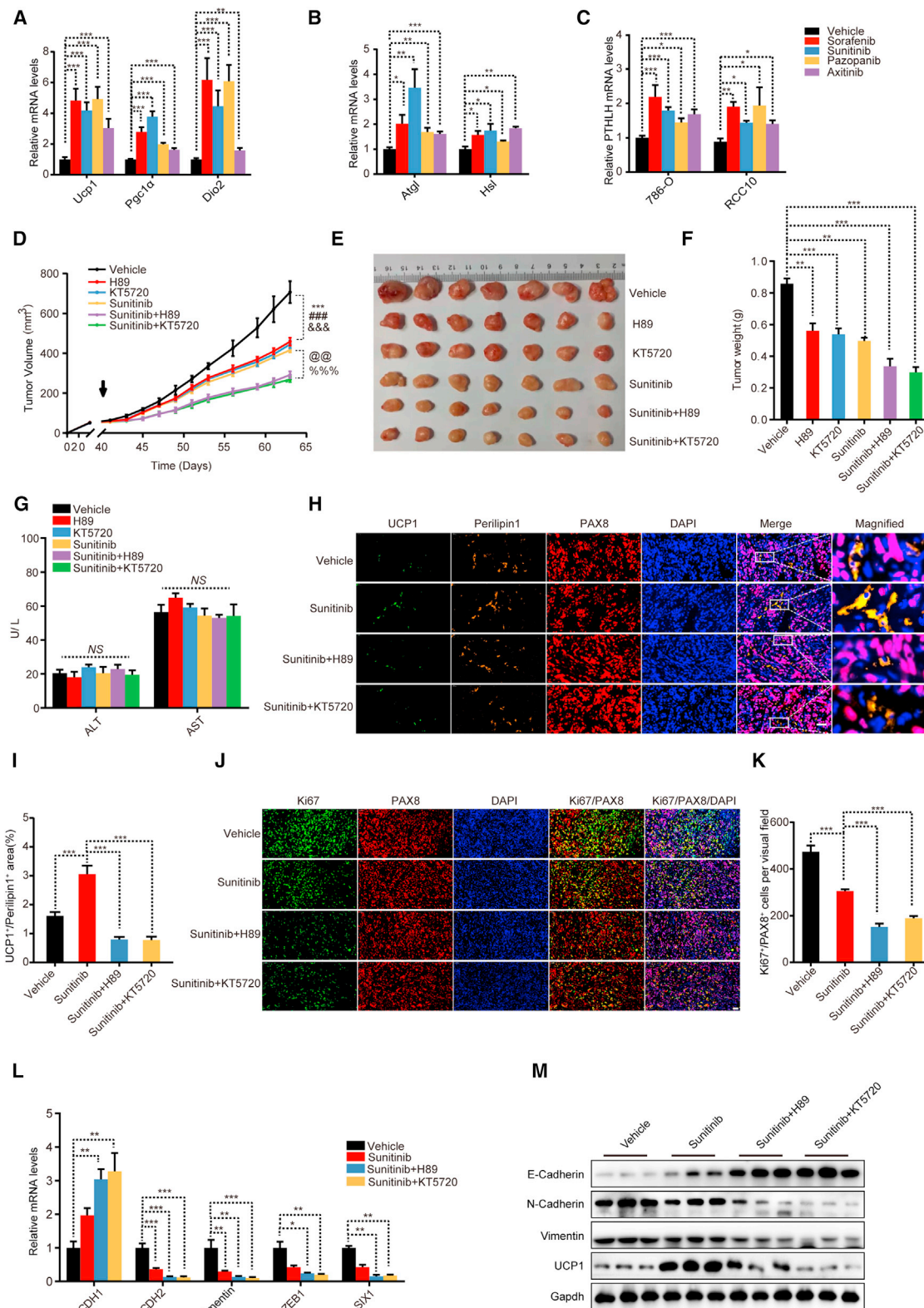
Figure 7. H89 and KT5720 blocked TKI-mediated browning of white adipocytes and augmented the anti-tumor efficacy of sunitinib *in vivo*

(A) Expression levels of genes related to browning in differentiated C3H10T1/2 cells after treatment with vehicle or TKIs: sorafenib (1 μM), sunitinib (2 μM), pazopanib (1 μM), or axitinib (1 μM) for 24 h (1 technical replicate of 3 biological replicates per group).

inhibiting adipocyte browning might limit tumor growth is by reducing the delivery, from beige adipocytes to ccRCC cells, of lactate. Through analyses of clinical samples, we found ccRCC tumors drove browning of adjacent fat, but not distal fat, indicating that tumor influence, and/or the benefit of reprogrammed adipocyte metabolism, is distance dependent and these observations suggest a paracrine pattern. In the current American and Chinese national clinical practice guidelines for the treatment of kidney cancer, there is no clear guidance on whether the paracancerous adipose tissue should be resected during ccRCC surgery (Motzer et al., 2019). Our findings in this study suggest that the removal of adjacent fat tissue might halt metabolite flow from beige adipocytes and improve post-surgical prognosis.

A number of tumors, such as breast, gastric, and ovarian cancers, tend to grow or undergo an EMT in the adipocyte-dominated TME; these tumors utilize FFAs released from adipocytes and are highly reliant on FAO for ATP production (Nieman et al., 2013; Martinez-Outschoorn et al., 2012; Snaebjornsson et al., 2020), whereas ccRCC exhibits a distinct metabolic pattern (Du et al., 2017). Similar to some other cancers, ccRCC tumors have the ability to take up FFAs. Even so, we found that the expression of FAO-related genes is suppressed in ccRCC. Compatible with this, the imported FFAs appeared to be re-esterified to form triglycerides, which was stored and condensed into large lipid droplets. Whether and how the accumulation of neutral triglycerides contributes to ccRCC cancer development remains to be investigated in the future. In contrast to FAO-related genes, the expression of genes involved in lactate transport (MCT1 and MCT4) and catabolism (LDHB) were higher in ccRCC cells than in normal renal cells, suggesting that lactate catabolism was higher in the tumors. We confirmed that lactate acts as a significant carbon source to fuel the TCA cycle of ccRCC cells. Consistently, in other cancers, lactate is preferred over glucose as a fuel for the TCA cycle (de la Cruz-López et al., 2019; Faubert et al., 2017). Meanwhile lactic acid also inhibits T cell activation and proliferation to favor tumor growth (Brisson et al., 2016; Ippolito et al., 2019).

We also found that four widely used TKIs—including sunitinib—all promoted the browning of white adipocytes and upregulated the expression of PTHrP in ccRCC tumor cells, which amplified the vicious cycle between ccRCC cells and adjacent adipocytes. This adverse effect might contribute to reduced TKI anti-tumor efficacy in clinical practice. Here, we validated that combination therapy involving TKIs and inhibitors of thermogenesis substantially improved the long-term efficacy of the TKI in reducing ccRCC tumor volume. Previously, only higher dosages of sunitinib (40 mg/kg or 20 mg/kg) showed obvious treatment efficacy against ccRCCs (Adelaiye-Ogala et al., 2018; Zhou et al., 2016). In this study when combined with browning inhibitors, a much lower dosage of sunitinib (10 mg/kg) strikingly suppressed tumor growth.

In summary, we identified a bi-directional communication between ccRCCs and the adjacent adipose tissue, which promoted ccRCC progression. Our data also revealed an adverse side effect of TKIs to promote PAT browning. Our study further verified that combination therapy with a TKI and thermogenesis inhibitors enhanced the anti-cancer efficacy of the former, expanding the arsenal of therapeutic agents for combating ccRCC.

Limitations of study

This study demonstrated that lactate is a significant fuel to support ccRCC cell growth in the ccRCC-PAT communication; however, other small molecules and regulatory pathways that may play critical roles in tumor growth remain to be investigated in the future. Regardless, FAO is suppressed in ccRCC, and FFAs could still be taken up and converted into triglycerides in ccRCC cells. The mechanism by which these lipids affect ccRCC tumorigenesis warrants further exploration. Furthermore, the specific features of ccRCC-induced PAT browning merits in-depth studies. Lastly, the detailed mechanism by which TKIs upregulate PTHLH in ccRCC cells, and how to counteract this disadvantage to improve their clinical efficacy, are key questions that remain to be elucidated.

(B) Expression levels of genes related to lipolysis in differentiated C3H10T1/2 cells after treatment with vehicle or sorafenib (2 μM), sunitinib (1 μM), pazopanib (1 μM) and axitinib (1 μM) for 24 h, respectively (1 technical replicate of 3 biological replicates per group).

(C) PTHLH mRNA levels in 786-O cells treated with vehicle or sorafenib (2 μM), sunitinib (1 μM), pazopanib (2 μM), and axitinib (1 μM), and in RCC10 cells treated with vehicle or sorafenib (1 μM), sunitinib (1 μM), pazopanib (1 μM), or axitinib (1 μM), respectively (1 technical replicate of 5–6 biological replicates per group).

(D) A subcutaneous tumor growth curve from 786-O cells (1×10^6 cells per mouse) mixed with BAC cells (0.25×10^6 cells per mouse) (n = 7 mice per group). The treatment with vehicle, H89, KT5720, sunitinib, H89 plus sunitinib, KT572 plus sunitinib began when volume of xenografts reached approximately 50 mm³. ***p < 0.001 in vehicle versus H89, ###p < 0.001 in vehicle versus KT5720, &&&p < 0.001 in vehicle versus sunitinib, @@p < 0.01 in sunitinib versus sunitinib + H89, %%%p < 0.001 in sunitinib versus sunitinib + KT5720. Arrow indicates initiation of drug treatment.

(E) Representative images of xenograft tumors in (D) at day 63 (n = 7 mice per group).

(F) Weights of xenograft tumors in (E) at day 63 (n = 7 mice per group).

(G) Serum ALT and AST levels of mice in (D) at day 63 (7 biological replicates per group).

(H) Representative mIHC images of xenograft tumors in (E) (6 images per 3 biological replicates for each group). Green, UCP1; orange, Perilipin1; red, PAX8; blue, DAPI. Scale bar, 50 μm.

(I) Proportions (%) of UCP1/Perilipin1 positive cells in (H) (6 images per 3 biological replicates for each group).

(J) Representative mIHC images of xenograft tumors in (E) (6 images per 3 biological replicates for each group). Green, Ki67; red, PAX8; blue, DAPI. Scale bar, 50 μm.

(K) Quantification of the average number of Ki67/PAX8 positive 786-O cells in (J) (6 images per 3 biological replicates for each group).

(L) Expression of EMT-related genes in xenograft tumors derived from (E) (1 technical replicate of 5 biological replicates for each group).

(M) Immunoblots of UCP1, E-cadherin, N-cadherin, and vimentin proteins in xenograft tumors derived from (E) (n = 3; representative of 3 biological replicates per group).

Data were expressed as means ± SEM. *p < 0.05, **p < 0.01, ***p < 0.001 by unpaired two-tailed Student's t tests (A–C), two-way ANOVA (D), or one-way ANOVA (F, G, I, K, and L).

Cell Metabolism
Article

STAR★METHODS

Detailed methods are provided in the online version of this paper and include the following:

- KEY RESOURCES TABLE
- RESOURCE AVAILABILITY
  - Lead contact
  - Materials availability
  - Data and code availability
- EXPERIMENTAL MODEL AND SUBJECT DETAILS
  - Mice and mice housing
  - Cell culture
- METHOD DETAILS
  - Biochemical reagents
  - Cell proliferation assay
  - Trans-well assays
  - Histological evaluation and immunohistochemistry
  - Immunofluorescence
  - RNA isolation and RT-qPCR
  - Western blotting
  - Plasmid constructs and lentivirus preparation
  - Determination of lactate content
  - Measurements of lipolysis *in vitro*
  - Measurement of mitochondrial copy number
  - MitoTracker staining
  - Seahorse XFe96 measurements
  - Metabolic flux assay
  - NMR and UPLC-ESI-MS/MS analysis
  - Lung metastasis assay
  - Orthotopic tumor growth
- QUANTIFICATION AND STATISTICAL ANALYSIS

SUPPLEMENTAL INFORMATION

Supplemental information can be found online at https://doi.org/10.1016/j.cmet.2021.08.012.

ACKNOWLEDGMENTS

AUTHOR CONTRIBUTIONS

DECLARATION OF INTERESTS

REFERENCES

Ackerman, D., Tumanov, S., Qiu, B., Michalopoulou, E., Spata, M., Azzam, A., Xie, H., Simon, M.C., and Kamphorst, J.J. (2018). Triglycerides promote lipid homeostasis during hypoxic stress by balancing fatty acid saturation. Cell Rep *24*, 2596–2605.e5.

Adelaiye-ogala, R., Damayanti, N.P., Orillion, A.R., Arisa, S., Chintala, S., Titus, M.A., Kao, C., and Pili, R. (2018). Therapeutic targeting of sunitinib-induced AR phosphorylation in renal cell carcinoma. Cancer Res *78*, 2886–2896.

Bartelt, A., and Heeren, J. (2014). Adipose tissue browning and metabolic health. Nat. Rev. Endocrinol. *10*, 24–36.

Bedke, J., Buse, S., Pritsch, M., Macher-Goeppinger, S., Schirmacher, P., Haferkamp, A., and Hohenfellner, M. (2009). Perinephric and renal sinus fat infiltration in pT3a renal cell carcinoma: possible prognostic differences. BJU Int *103*, 1349–1354.

Brestoff, J.R., and Artis, D. (2015). Immune regulation of metabolic homeostasis in health and disease. Cell *161*, 146–160.

Brisson, L., Bański, P., Sboarina, M., Dethier, C., Danhier, P., Fontenille, M.J., Van Hée, V.F., Vazeille, T., Tardy, M., Falces, J., et al. (2016). Lactate dehydrogenase B controls lysosome activity and autophagy in cancer. Cancer Cell *30*, 418–431.

Calton, E.K., Keane, K.N., Soares, M.J., Rowlands, J., and Newsholme, P. (2016). Prevailing vitamin D status influences mitochondrial and glycolytic bioenergetics in peripheral blood mononuclear cells obtained from adults. Redox Biol *10*, 243–250.

Carter, J.C., and Church, F.C. (2012). Mature breast adipocytes promote breast cancer cell motility. Exp. Mol. Pathol. *92*, 312–317.

Chandrashekar, D.S., Bashel, B., Balasubramanya, S.A.H., Creighton, C.J., Ponce-Rodriguez, I., Chakravarthi, B.V.S.K., and Varambally, S. (2017). UALCAN: a portal for facilitating tumor subgroup gene expression and survival analyses. Neoplasia *19*, 649–658.

Chen, S., Liu, X., Peng, C., Tan, C., Sun, H., Liu, H., Zhang, Y., Wu, P., Cui, C., Liu, C., et al. (2021). The phytochemical hyperforin triggers thermogenesis in adipose tissue via a Dlat-AMPK signaling axis to curb obesity. Cell Metab *33*, 565–580.e7.

Chrysovergis, K., Wang, X., Kosak, J., Lee, S.-H., Kim, J.S., Foley, J.F., Travlos, G., Singh, S., Baek, S.J., and Eling, T.E. (2014). NAG-1/GDF-15 prevents obesity by increasing thermogenesis, lipolysis and oxidative metabolism. Int. J. Obes. (Lond.). *38*, 1555–1564.

Dai, H., Xiao, C., Liu, H., and Tang, H. (2010). Combined NMR and LC-MS analysis reveals the metabonomic changes in Salvia miltiorrhiza Bunge induced by water depletion. J. Proteome Res. *9*, 1460–1475.

de la Cruz-López, K.G., Castro-Muñoz, L.J., Reyes-Hernández, D.O., García-Carrancá, A., and Manzo-Merino, J. (2019). Lactate in the regulation of tumor microenvironment and therapeutic approaches. Front. Oncol. *9*, 1143.

De Palma, M., Biziato, D., and Petrova, T.V. (2017). Microenvironmental regulation of tumour angiogenesis. Nat. Rev. Cancer *17*, 457–474.

Du, W., Zhang, L., Brett-Morris, A., Aguila, B., Kerner, J., Hoppel, C.L., Puchowicz, M., Serra, D., Herrero, L., Rini, B.I., et al. (2017). HIF drives lipid deposition and cancer in ccRCC via repression of fatty acid metabolism. Nat. Commun. *8*, 1769.

Elattar, S., Dimri, M., and Satyanarayana, A. (2018). The tumor secretory factor ZAG promotes white adipose tissue browning and energy wasting. FASEB J *32*, 4727–4743.

Faubert, B., Li, K.Y., Cai, L., Hensley, C.T., Kim, J., Zacharias, L.G., Yang, C., Do, Q.N., Doucette, S., Burguete, D., et al. (2017). Lactate metabolism in human lung tumors. Cell *171*, 358–371.e9.

Fiaschi, T., Marini, A., Giannoni, E., Taddei, M.L., Gandellini, P., De Donatis, A., Lanciotti, M., Serni, S., Cirri, P., and Chiarugi, P. (2012). Reciprocal metabolic reprogramming through lactate shuttle coordinately influences tumor-stroma interplay. Cancer Res *72*, 5130–5140.

Galarraga, M., Campión, J., Muñoz-Barrutia, A., Boqué, N., Moreno, H., Martínez, J.A., Milagro, F., and Ortiz-de-Solórzano, C. (2012). Adiposoft: automated software for the analysis of white adipose tissue cellularity in histological sections. J. Lipid Res. *53*, 2791–2796.

Goossens, P., Rodriguez-Vita, J., Etzerodt, A., Masse, M., Rastoin, O., Gouirand, V., Ulas, T., Papantonopoulou, O., Van Eck, M., Auphan-Anezin, N., et al. (2019). Membrane cholesterol efflux drives tumor-associated macrophage reprogramming and tumor progression. Cell Metab *29*, 1376–1389.e4.

Huang, X.Y., Huang, Z.L., Yang, J.H., Xu, Y.H., Sun, J.S., Zheng, Q., Wei, C., Song, W., and Yuan, Z. (2016). Pancreatic cancer cell-derived IGFBP-3 contributes to muscle wasting. J. Exp. Clin. Cancer Res. *35*, 46.

Ippolito, L., Morandi, A., Giannoni, E., and Chiarugi, P. (2019). Lactate: a metabolic driver in the tumour landscape. Trends Biochem. Sci. *44*, 153–166.

Iwamoto, H., Abe, M., Yang, Y., Cui, D., Seki, T., Nakamura, M., Hosaka, K., Lim, S., Wu, J., He, X., et al. (2018). Cancer lipid metabolism confers antiangiogenic drug resistance. Cell Metab *28*, 104–117.e5.

Jespersen, N.Z., Feizi, A., Andersen, E.S., Heywood, S., Hattel, H.B., Daugaard, S., Peijs, L., Bagi, P., Feldt-Rasmussen, B., Schultz, H.S., et al. (2019). Heterogeneity in the perirenal region of humans suggests presence of dormant brown adipose tissue that contains brown fat precursor cells. Mol. Metab. *24*, 30–43.

Kiefer, F.W., Vernochet, C., O'Brien, P., Spoerl, S., Brown, J.D., Nallamshetty, S., Zeyda, M., Stulnig, T.M., Cohen, D.E., Kahn, C.R., and Plutzky, J. (2012). Retinaldehyde dehydrogenase 1 regulates a thermogenic program in white adipose tissue. Nat. Med. *18*, 918–925.

Kir, S., White, J.P., Kleiner, S., Kazak, L., Cohen, P., Baracos, V.E., and Spiegelman, B.M. (2014). Tumour-derived PTH-related protein triggers adipose tissue browning and cancer cachexia. Nature *513*, 100–104.

Li, P., Oh, D.Y., Bandyopadhyay, G., Lagakos, W.S., Talukdar, S., Osborn, O., Johnson, A., Chung, H., Maris, M., Ofrecio, J.M., et al. (2015). LTB4 promotes insulin resistance in obese mice by acting on macrophages, hepatocytes and myocytes. Nat. Med. *21*, 239–247.

Li, B., Qiu, B., Lee, D.S., Walton, Z.E., Ochocki, J.D., Mathew, L.K., Mancuso, A., Gade, T.P., Keith, B., Nissim, I., et al. (2014). Fructose-1,6-bisphosphatase opposes renal carcinoma progression. Nature *513*, 251–255.

Maguire, O.A., Ackerman, S.E., Szwed, S.K., Maganti, A.V., Marchildon, F., Huang, X., Kramer, D.J., Rosas-Villegas, A., Gelfer, R.G., Turner, L.E., et al. (2021). Creatine-mediated crosstalk between adipocytes and cancer cells regulates obesity-driven breast cancer. Cell Metab *33*, 499–512.e6.

Mao, L., Nie, B., Nie, T., Hui, X., Gao, X., Lin, X., Liu, X., Xu, Y., Tang, X., Yuan, R., et al. (2017). Visualization and quantification of browning using a Ucp1-2A-Luciferase knock-in mouse model. Diabetes *66*, 407–417.

Martinez-Outschoorn, U.E., Sotgia, F., and Lisanti, M.P. (2012). Power surge: supporting cells "fuel" cancer cell mitochondria. Cell Metab *15*, 4–5.

Motzer, R.J., Jonasch, E., Michaelson, M.D., Nandagopal, L., Gore, J.L., George, S., Alva, A., Haas, N., Harrison, M.R., Plimack, E.R., et al. (2019). NCCN Guidelines Insights: Kidney Cancer, Version 2.2020. J. Natl. Compr. Canc. Netw. *17*, 1278–1285.

Nguyen, H.P., Yi, D., Lin, F., Viscarra, J.A., Tabuchi, C., Ngo, K., Shin, G., Lee, A.Y., Wang, Y., and Sul, H.S. (2020). Aifm2, a NADH oxidase, supports robust glycolysis and is required for cold- and diet-induced thermogenesis. Mol. Cell *77*, 600–617.e4.

Nieman, K.M., Kenny, H.A., Penicka, C.V., Ladanyi, A., Buell-Gutbrod, R., Zillhardt, M.R., Romero, I.L., Carey, M.S., Mills, G.B., Hotamisligil, G.S., et al. (2011). Adipocytes promote ovarian cancer metastasis and provide energy for rapid tumor growth. Nat. Med. *17*, 1498–1503.

Nieman, K.M., Romero, I.L., Van Houten, B., and Lengyel, E. (2013). Adipose tissue and adipocytes support tumorigenesis and metastasis. Biochim. Biophys. Acta *1831*, 1533–1541.

Okamatsu-Ogura, Y., Kuroda, M., Tsutsumi, R., Tsubota, A., Saito, M., Kimura, K., and Sakaue, H. (2020). UCP1-dependent and UCP1-independent metabolic changes induced by acute cold exposure in brown adipose tissue of mice. Metabolism *113*, 154396.

Okhunov, Z., Mues, A.C., Kline, M., Haramis, G., Xu, B., Mirabile, G., Vira, M., and Landman, J. (2012). Evaluation of perirenal fat as a predictor of cT 1a renal cortical neoplasm histopathology and surgical outcomes. J. Endourol. *26*, 911–916.

Petruzzelli, M., Schweiger, M., Schreiber, R., Campos-Olivas, R., Tsoli, M., Allen, J., Swarbrick, M., Rose-John, S., Rincon, M., Robertson, G., et al. (2014). A switch from white to brown fat increases energy expenditure in cancer-associated cachexia. Cell Metab *20*, 433–447.

Qiu, B., Ackerman, D., Sanchez, D.J., Li, B., Ochocki, J.D., Grazioli, A., Bobrovnikova-Marjon, E., Diehl, J.A., Keith, B., and Simon, M.C. (2015). HIF2alpha-dependent lipid storage promotes endoplasmic reticulum homeostasis in clear-cell renal cell carcinoma. Cancer Discov *5*, 652–667.

Qiu, Y., Sun, Y., Xu, D., Yang, Y., Liu, X., Wei, Y., Chen, Y., Feng, Z., Li, S., Reyad-Ul Ferdous, M., et al. (2018). Screening of FDA-approved drugs identifies sutent as a modulator of UCP1 expression in brown adipose tissue. EBiomedicine *37*, 344–355.

Qu, L., Ding, J., Chen, C., Wu, Z.J., Liu, B., Gao, Y., Chen, W., Liu, F., Sun, W., Li, X.F., et al. (2016). Exosome-transmitted lncARSR promotes sunitinib resistance in renal cancer by acting as a competing endogenous RNA. Cancer Cell *29*, 653–668.

Rini, B.I., and Atkins, M.B. (2009). Resistance to targeted therapy in renal-cell carcinoma. Lancet Oncol *10*, 992–1000.

Sanjana, N.E., Shalem, O., and Zhang, F. (2014). Improved vectors and genome-wide libraries for CRISPR screening. Nat. Methods *11*, 783–784.

Schneider, C.A., Rasband, W.S., and Eliceiri, K.W. (2012). NIH Image to ImageJ: 25 years of image analysis. Nat. Methods *9*, 671–675.

Shah, P.H., Lyon, T.D., Lohse, C.M., Cheville, J.C., Leibovich, B.C., Boorjian, S.A., and Thompson, R.H. (2019). Prognostic evaluation of perinephric fat, renal sinus fat, and renal vein invasion for patients with pathological stage T3a clear-cell renal cell carcinoma. BJU Int *123*, 270–276.

Shamsi, F., Xue, R., Huang, T.L., Lundh, M., Liu, Y., Leiria, L.O., Lynes, M.D., Kempf, E., Wang, C.H., Sugimoto, S., et al. (2020). FGF6 and FGF9 regulate UCP1 expression independent of brown adipogenesis. Nat. Commun. *11*, 1421.

Snaebjornsson, M.T., Janaki-Raman, S., and Schulze, A. (2020). Greasing the wheels of the cancer machine: the role of lipid metabolism in cancer. Cell Metab *31*, 62–76.

Tews, D., Pula, T., Funcke, J.B., Jastroch, M., Keuper, M., Debatin, K.M., Wabitsch, M., and Fischer-Posovszky, P. (2019). Elevated UCP1 levels are sufficient to improve glucose uptake in human white adipocytes. Redox Biol *26*, 101286.

Tsao, C.K., Liaw, B., He, C., Galsky, M.D., Sfakianos, J., and Oh, W.K. (2017). Moving beyond vascular endothelial growth factor-targeted therapy in renal cell cancer: latest evidence and therapeutic implications. Ther. Adv. Med. Oncol. *9*, 287–298.

Wan, Q., Wang, Y., and Tang, H. (2017). Quantitative 13C traces of glucose fate in hepatitis B virus-infected hepatocytes. Anal. Chem. *89*, 3293–3299.

Wang, Y.Y., Attané, C., Milhas, D., Dirat, B., Dauvillier, S., Guerard, A., Gilhodes, J., Lazar, I., Alet, N., Laurent, V., et al. (2017). Mammary adipocytes stimulate breast cancer invasion through metabolic remodeling of tumor cells. JCI Insight *2*, e87489.

Wei, G., Sun, H., Liu, J.L., Dong, K., Liu, J., and Zhang, M. (2020). Indirubin, a small molecular deriving from connectivity map (CMAP) screening, ameliorates obesity-induced metabolic dysfunction by enhancing brown adipose thermogenesis and white adipose browning. Nutr. Metab. (Lond.) *17*, 21.

Weir, G., Ramage, L.E., Akyol, M., Rhodes, J.K., Kyle, C.J., Fletcher, A.M., Craven, T.H., Wakelin, S.J., Drake, A.J., Gregoriades, M.L., et al. (2018). Substantial metabolic activity of human brown adipose tissue during warm conditions and cold-induced lipolysis of local triglycerides. Cell Metab *27*, 1348–1355.e4.

Wen, Y.A., Xing, X., Harris, J.W., Zaytseva, Y.Y., Mitov, M.I., Napier, D.L., Weiss, H.L., Mark Evers, B., and Gao, T. (2017). Adipocytes activate mitochondrial fatty acid oxidation and autophagy to promote tumor growth in colon cancer. Cell Death Dis *8*, e2593.

Wettersten, H.I., Hakimi, A.A., Morin, D., Bianchi, C., Johnstone, M.E., Donohoe, D.R., Trott, J.F., Aboud, O.A., Stirdivant, S., Neri, B., et al. (2015). Grade-dependent metabolic reprogramming in kidney cancer revealed by combined proteomics and metabolomics analysis. Cancer Res *75*, 2541–2552.

Wu, X., Li, N., Li, H., and Tang, H. (2014). An optimized method for NMR-based plant seed metabolomic analysis with maximized polar metabolite extraction efficiency, signal-to-noise ratio, and chemical shift consistency. Analyst *139*, 1769–1778.

Wu, N.N., Zhang, C.H., Lee, H.J., Ma, Y., Wang, X., Ma, X.J., Ma, W., Zhao, D., and Feng, Y.M. (2016). Brown adipogenic potential of brown adipocytes and peri-renal adipocytes from human embryo. Sci. Rep. *6*, 39193.

Xiao, C., Hao, F., Qin, X., Wang, Y., and Tang, H. (2009). An optimized buffer system for NMR-based urinary metabonomics with effective pH control, chemical shift consistency and dilution minimization. Analyst *134*, 916–925.

Xu, K.Y., and Wu, S. (2015). Update on the treatment of metastatic clear cell and non-clear cell renal cell carcinoma. Biomark. Res. *3*, 5.

Yuan, X., Wei, G., You, Y., Huang, Y., Lee, H.J., Dong, M., Lin, J., Hu, T., Zhang, H., Zhang, C., et al. (2017). Rutin ameliorates obesity through brown fat activation. FASEB J *31*, 333–345.

Zarrabi, K., Fang, C., and Wu, S. (2017). New treatment options for metastatic renal cell carcinoma with prior anti-angiogenesis therapy. J. Hematol. Oncol. *10*, 38.

Zhang, W., Hubbard, A., Jones, T., Racolta, A., Bhaumik, S., Cummins, N., Zhang, L., Garsha, K., Ventura, F., Lefever, M.R., et al. (2017). Fully automated 5-plex fluorescent immunohistochemistry with tyramide signal amplification and same species antibodies. Lab. Invest. *97*, 873–885.

Zhao, X.Y., Li, S., Wang, G.X., Yu, Q., and Lin, J.D. (2014). A long noncoding RNA transcriptional regulatory circuit drives thermogenic adipocyte differentiation. Mol. Cell *55*, 372–382.

Zhou, L., Liu, X.D., Sun, M., Zhang, X., German, P., Bai, S., Ding, Z., Tannir, N., Wood, C.G., Matin, S.F., et al. (2016). Targeting MET and AXL overcomes resistance to sunitinib therapy in renal cell carcinoma. Oncogene *35*, 2687–2697.

STAR★METHODS

KEY RESOURCES TABLE

REAGENT or RESOURCE	SOURCE	IDENTIFIER
Antibodies		
Rabbit polyclonal I anti-UCP1, dil:1/1000	Abcam	Cat# ab23841; RRID: AB_2213764
		Cat# ab10983; RRID: AB_2241462
Rabbit monoclonal anti-Total OXPHOS Rodent WB Antibody Cocktail, dil:1/500	Abcam	Cat# ab110413; RRID: AB_2629281
Rabbit polyclonal anti-PKA-Cα/β, dil:1/1,000	Abcam	Cat# ab71764; RRID: AB_1269777
Rabbit polyclonal anti-Phospho-HSL (Ser660), dil:1/1,000	Cell Signaling Technology	Cat# 4126; RRID: AB_490997
Rabbit polyclonal anti-HSL, dil:1/1,000	Cell Signaling Technology	Cat# 4107; RRID: AB_2296900
Rabbit monoclonal anti-CREB (48H2), dil:1/1,000	Cell Signaling Technology	Cat# 9197; RRID: AB_331277
Rabbit monoclonal anti-Phospho-CREB (Ser133) (87G3), WB, dil:1/1,000	Cell Signaling Technology	Cat# 9198; RRID: AB_2561044
Rabbit monoclonal anti-Phospho-PKA Substrate (RRXS*/T*) (100G7E), dil:1/1,000	Cell Signaling Technology	Cat# 9624; RRID: AB_331817
Rabbit monoclonal anti-PAX8 (D2S2I), dil:1/200	Cell Signaling Technology	Cat# 59019; RRID: AB_2799553
Rabbit monoclonal anti-Perilipin1 (D1D8), dil:1/200	Cell Signaling Technology	Cat# 9349; RRID: AB_10829911
Rabbit monoclonal anti-α-Actinin (D6F6), dil:1/1,000	Cell Signaling Technology	Cat# 6487; RRID: AB_11179206
Rabbit polyclonal anti-β-Tubulin, dil:1/1,000	Cell Signaling Technology	Cat# 8457; RRID: AB_2210545
Rabbit monoclonal anti-GAPDH (D16H11), dil:1/1,000	Cell Signaling Technology	Cat# 5174; RRID: AB_10622025
Rabbit polyclonal anti-HSP90, dil:1/1,000	Cell Signaling Technology	Cat# 4874; RRID: AB_2121214
Rabbit monoclonal anti-N-Cadherin (D4R1H) XP , dil:1/1,000	Cell Signaling Technology	Cat# 13116; RRID: AB_2687616
Rabbit monoclonal anti-E-Cadherin (24E10) XP , dil:1/1,000	Cell Signaling Technology	Cat# 3195; RRID: AB_2291471
Rabbit monoclonal anti-vimentin (D21H3) XP, dil:1/1,000	Cell Signaling Technology	Cat# 5741; RRID: AB_10695459
Rabbit polyclonal anti-CD36, dil:1/1,000	Absin, china.	Cat# abs120668
Rabbit polyclonal anti-PTHR, dil:1/1,000	Absin, china.	Cat# abs135215
Rabbit polyclonal anti-MCT1, dil:1/1,000	Absin, china.	Cat# abs120479
Rabbit polyclonal anti-MCT4, dil:1/1,000	Absin, china.	Cat# abs124388
Mouse monoclonal anti-PTHrP (1-34) antibody (clone 23-57-137-1), dil:1:500	Millipore	Cat# MABN793
Normal mouse IgG, dil:1:500	Santa Cruz	Cat# sc-2025; RRID: AB_737182
Peroxidase AffiniPure Goat Anti-Rabbit IgG (H+L), dil:1/5,000	Jackson ImmunoResearch	Cat# Fs111-035-003; RRID: AB_2313567
Peroxidase AffiniPure Goat Anti-Mouse IgG(H+L), dil:1/5,000	Jackson ImmunoResearch	Cat# Fs115-035-003; RRID: AB_10015289

(*Continued on next page*)

Continued

REAGENT or RESOURCE	SOURCE	IDENTIFIER
Biological samples		
Human normal kidney tissue sample	Yan'an Affiliated Hospital of Kunming Medical University	N/A
Human ccRCC tissue sample	Yan'an Affiliated Hospital of Kunming Medical University	N/A
Chemicals, peptides, and recombinant proteins		
Sunitinib	MedChemExpress	Cat# HY-10255A
Pazopanib	MedChemExpress	Cat# HY10208
Sorafenib	MedChemExpress	Cat# HY-10201
Axitinib	MedChemExpress	Cat# HY-10065
7ACC1	MedChemExpress	Cat# HY-D0067
H89	MedChemExpress	Cat# HY-15979
KT5720	MedChemExpress	Cat# HY-N6789
Dimethyl sulfoxide (DMSO)	Sigma-Aldrich	Cat 2650
Corn oil	Sigma-Aldrich	Cat 394906
Cremophor El	Sigma-Aldrich	Cat 238470
Dimethyl-acetoacetamide (DMA)	Sigma-Aldrich	Cat 394906
Oil Red O	Sigma-Aldrich	Cat# O0625
3-isobutyl-1-methylxanthine	Sigma-Aldrich	Cat# I7018
Indomethacin	Sigma-Aldrich	Cat# I7378
Dexamethasone	Sigma-Aldrich	Cat# D4902
Insulin	Sigma-Aldrich	Cat# I-5500
Triiodothyronine (T3)	Sigma-Aldrich	Cat# t-2752
Rosiglitazone	Sigma-Aldrich	Cat# R2408
DMEM	ThermoFisher Scientific	Cat# C11995500BT
Opti-MEM I Reduced Serum Medium	Thermo Fisher Scientific	Cat# 31985062
Fetal Bovine Serum	ThermoFisher Scientific	Cat 16000-044
Calf serum	Selborne Biological Services	Cat# 1491
Penicillin/Streptomycin	ThermoFisher Scientific	Cat# 15140-122
Lipofectamine 3000 Transfection Reagent	ThermoFisher Scientific	Cat# L3000015
TRIzol reagent	ThermoFisher Scientific	Cat# 15596
Trypsin	ThermoFisher Scientific	Cat# 25200
PTHrP (1-34) peptides	GLBiochem, China	Cat# 101859
Sodium L-lactate ($^{13}C_3$, 98%)	Cambridge Isotope Laboratories	Cat# CLM-1579-0
Critical commercial assays		
BCA assay kit	Thermo Fisher Scientific	Cat# 23225
MitoTracker Red probe	ThermoFisher Scientific	Cat# M7512
Hiscript II reverse transcriptase	Vazyme, China	Cat# R222-01-AB
SYBR-green PCR mix	Vazyme, China	Cat# Q511-02
LabAssay NEFA	Wako diagnostics	Cat# 294-63601
EnzyChrom Adipolysis Assay Kit	BioAssay Systems	Cat# EAPL-200
XF Cell Mito Stress Test Kit	Agilent Technologies	Cat# 103015-100
Palmitate-BSA FAO Substrate	Agilent Technologies	Cat# 102720-100
Fluorescent multiplex immunohistochemistry (mIHC) kit	Absin, china	Cat# abs50013
The PTHrP (1–34) enzyme-linked immunosorbent assay (ELISA)	Phoenix Pharmaceuticals	Cat# S-1227
BCA Protein assay kit	Thermo Fisher Scientific	Cat 23225
EasyPure Genomic DNA kit	Transgen Biotech	Cat# EE101

(Continued on next page)

Continued

REAGENT or RESOURCE	SOURCE	IDENTIFIER
Experimental models: Cell lines		
Mouse: C3H10T1/2 cells	ATCC	Cat# CCL-226
Mouse: 3T3L1 cells	ATCC	Cat# CL-173
Mouse: Primary inguinal adipocytes	This paper	N/A
Mouse: Primary brown adipocytes	This paper	N/A
Mouse: Immortalized brown and beige pre-adipocytes	Zhao et al., 2014	N/A
Human:786-O cells	ATCC	Cat# CRL-1932
Human: RCC10 cells	(Li et al., 2014)	N/A
Human: HK2 cells	ATCC	Cat# CRL-2190
Human: HEK293 cells	ATCC	Cat# CRL-1573
Experimental models: Organisms/strains		
Mouse strain: B-NDG (B-NDG)	Biocytogen	Cat# 110586
Mouse strain: BALB/c-Nu	GemPharmatech	Cat# D000521
Oligonucleotides		
Primers for RT-qPCR, see Table S2	This paper	N/A
Sequences for shRNA primers, see Table S3	This paper	N/A
sgRNA target sequences for CRISPR-Cas9, see Table S3	This paper	N/A
Recombinant DNA		
pLKO.1-puro	Addgene	Cat# 8453
pMD2.G	Addgene	Cat# 12259
psPAX2	Addgene	Cat# 12260
pCDH-GFP	Addgene	Cat# 72263
pCDH-mCherry	Addgene	Cat# 129440
lenti-CRISPR-V2	Addgene	Cat# 52961
Software and algorithms		
GraphPad Prism V8	GraphPad Software	https://www.graphpad.com/
ImageJ	(Schneider et al., 2012)	https://imagej.nih.gov/ij/
Adobe Photoshop	Adobe	https://www.adobe.com/
Adiposoft software	Galarraga et al., 2012	https://imagej.net/plugins/adiposoft
Other		
Mouse chow diet	SLACOM	Cat# P1101F-25
PVDF membrane	Millipore	Cat# IPVH00010
0.45 μm filter	Millipore	Cat# SLHV033RB
100 μm mesh filter	Falcon	Cat# 352360
40 μm mesh filter	Falcon	Cat# 352340

RESOURCE AVAILABILITY

Lead contact
Further information and requests for resources and reagents should be directed to and will be fulfilled by the Lead Contact, Junli Liu (liujunli@sjtu.edu.cn).

Materials availability
Plasmids generated in this study are available from the lead contact upon request. This study did not generate new unique reagents.

Data and code availability
- All data reported in this paper will be shared by the lead contact upon request.
- This paper does not report original code.
- Any additional information required to reanalyze the data reported in this paper is available from the lead contact upon request.

EXPERIMENTAL MODEL AND SUBJECT DETAILS

Mice and mice housing

Male B-NDG (B-NDG) mice (B:Biocytogen; N:NOD background; D:DNAPK (Prkdc) null; G:IL2rg knockout) mice (aged 4 to 6 weeks) and BALB/c nude mice (aged 4 to 6 weeks) were obtained from Beijing Biocytogen and GemPharmatech, respectively. The animals were maintained at room temperature (22-25°C) and with free access to food and water with 12 h light/dark cycle. All mice used in experiments throughout the study exhibited normal health. All mice were used after 1- or 2-weeks acclimatization after importing into the facility. All protocols were approved by the Institutional Animal Care and Use Committee at SIBCB of the Chinese Academy of Sciences (Shanghai, China) (SIBCB-S373-1901-003; SIBCB-S373-1809-027). For subcutaneous xenograft studies, 786-O cells (1 x 10^6 cells) were mixed with PBS or C3H10T1/2 cells or BAC cells (0.25 x 10^6 cells) at a ratio of 4:1 and implanted subcutaneously into the right flank of the mice with Matrigel in 100 μL (Corning, #354234). For comparison of the effects between white and beige fat cells on tumor growth, 3T3L1 and C3H10T1/2 cells were differentiated into matured white or beige adipocytes (0.25 x 10^6 cells) and were co-injected together with 786-O cells (1 x 10^6 cells) into B-NDG mice in the same way. To monitor tumor growth, the tumor diameter was measured every 2 or 3 days with a digital caliper. The tumor volumes were defined as 0.5 × (longest diameter) × (shortest diameter) × (shortest diameter). To assess the improved efficacy of sunitinib by inhibiting the browning of adipocytes with H89 or KT5720, mice were randomly assigned into different groups when the xenografts reached approximately 50 or 100 mm^3 and were then administered different treatments. At the end of experiments, tumors dissected from individual mice were weighed, fixed in 4% paraformaldehyde or flash frozen under liquid nitrogen.

Cell culture

Adipocyte culture and differentiation

Inguinal subcutaneous and perirenal WAT stromal-vascular fraction (SVF) cells were routinely isolated from male (aged 4 to 6 weeks) mice, cultured and differentiated into matured adipocytes following the previous published method (Kir et al., 2014) with slight modifications. Briefly, the inguinal and perirenal white fat pads were obtained from 6-week-old male mice, and then dissected, washed twice with 1 x phosphate-buffered saline (PBS) (Sigma), minced into small pieces and digested for 40 min at 37°C in an isolation buffer containing antibiotics (2.5 μg/mL fungizone, 50 μg/mL gentamicin, 1% pen/strep), 1 mg/mL collagenase I (Sigma) and 1% bovine serum albumin (BSA) (Sigma). Digested tissues were passed through a sterile 100-μm nylon mesh (BD Falcon) to remove undigested parts and centrifuged the remaining suspension at 500×g for 5 min to generate SVF cells in the pellet. The pellet was resuspended in DMEM/F12 (Invitrogen) medium containing 1% pen/strep and 10% FBS, passed through a 40-μm nylon mesh, centrifuged, resuspended (as described above), and plated on collagen-coated culture dishes (Corning). When the SVF cells were grown to confluence, pre-adipocyte differentiation (day 0) was induced by an adipogenic cocktail containing 1 μM rosiglitazone, 5 μg/mL insulin, 1 μM dexamethasone, 0.5 mM isobutylmethylxanthine for two days. The cells were then maintained in growth medium containing 1 μM rosiglitazone, 5 μg/mL insulin for two more days. The cells were switched to fresh growth medium for additional two days. By day 6, the mature adipocytes were treated with various conditioned media, chemicals or PTHrP for indicated time before harvesting.

The interscapular BAT SVF cells (sex unknown) were obtained from newborn mice (within postnatal 48 h), which were then minced into small pieces and digested for 30 min at 37°C in an isolation buffer containing 1.5 mg/mL collagenase I (Sigma), 100 mM HEPES, 5.0 mM glucose, 5 mM KCl, 1.3 mM $CaCl_2$, 123 mM NaCl, 1% pen/strep and 4% BSA. Digested tissues were passed through a sterile 100-μm nylon mesh (BD Falcon) to remove undigested parts and centrifuged the remaining suspension at 500×g for 10 min. The pelleted SVF cells were resuspended in DMEM (high glucose) plus 20% FBS, and 1% pen/strep, which then were plated and grown to confluence prior to induction for adipocyte differentiation. Immortalized brown and beige lines (BAC) (sex unknown) were obtained by infection with the retrovirus encoding SV40T antigen, which were kindly provided by Professor Jiandie D, Lin in USA (Life Sciences Institute and Department of Cell & Developmental Biology, University of Michigan Medical Center) (Zhao et al., 2014). For adipocyte differentiation, cells were cultured to confluence and incubated with DMEM (high glucose) plus 10% FBS, 0.125 mM indomethacin, 1 nM triiodothyronine (T3), 20 nM insulin, 5 μM dexamethasone and 0.5 mM isobutylmethylxanthine (Sigma). The cells were then maintained in growth medium containing 1 nM T3 and 20 nM insulin for an additional four days. By day 6, the mature adipocytes were switched to growth medium and treated with various conditioned media, chemicals or PTHrP for 24 h before harvesting. Mouse mesenchymal cell lines C3H10T1/2 (ATCC-CCL-226; sex unknown) and 3T3L1 pre-adipocytes (ATCC-CL-173; sex unknown) were routinely cultured in DMEM (high glucose) medium containing 10% FBS (Gibco, Thermo Fisher Scientific, USA) and 10% neonatal calf serum (CS) (Selborne Biological Services, Tasmania, Australia), respectively. The induction procedures of C3H10T1/2 and 3T3L1 cells to matured beige cells were almost the same as those of BAT SVF cells, exept for extra 1 μM rosiglitazone in adipogenic cocktail during the first two days. The identity of 3T3L1 cells was recently authenticated by STR and all the cells were routinely screened for mycoplasma absence.

Human ccRCC cell culture and CM preparation

Human ccRCC cell lines 786-O (ATCC-CRL-1932; sex: male), RCC10 (sex unknown) (a kind gift from Dr. Bo Li, Sun Yat-Sen University, China) (Li et al., 2014), together with human renal tubular epithelial cell line HK2 (ATCC-CRL-2190; sex: male) were cultured in DMEM (high glucose) containing 10% FBS and 1% pen/strep. All the cells were routinely screened for mycoplasma absence. For CM collection, 786-O, RCC10 and HK2 cells were plated the day before and the media were changed to FreeStyle expression medium (12338026; Gibco, Thermo Fisher Scientific, USA) next day. The CM from 786-O (786-O-CM), RCC10 (RCC10-CM) and HK2 (HK2-CM) were collected 24 h later, centrifuged at 1500×g for 5 min, and filtered through a 0.22-μm filter. Mature, differentiated adipocytes

were exposed to fresh media mixed with CM from ccRCC or HK2 cells at a ratio of 1:1 (v/v) for 24h. For two-step CM transfer experiments, the CM were replaced with fresh culture medium, and 24 h later the supernatant from the adipocytes (i.e., adipocyte CM) were collected, centrifuged as above, and filtered using a 0.22-μm filter, then mixed with fresh culture medium at 1:1 ratio culture medium and applied to treat 786-O or RCC10 cells for 24h for *in vitro* proliferation and migration assays.

Human samples

The procedures were approved by the Ethics Board at Kunming Medical University (approval no. 2019-047-01) and was registered in Chinese Clinical Trial Registration (trial registration identifier: ChiCTR1900025504). Study participants with clinical diagnosis of ccRCC undergoing nephrectomy were given informed consent. The adipose tissue adherent to the tumor or farther away (>5 cm) from the tumor were obtained from 54 individuals with ccRCC during the surgery. The clinical characteristics of study participants including sex, age, race, BMI were collected (Table S1). Exclusion criteria were if the study participants had received previous chemotherapy or pathological diagnosis of non-clear cell RCC. Tissue obtained were fixed with 4% paraformaldehyde or flash frozen under liquid nitrogen.

METHOD DETAILS

Biochemical reagents

The TKIs (axitinib, sorafenib, sunitinib, pazopanib) and PKA inhibitors (H89 and KT5720) were purchased from MedChemExpress (Monmouth Junction, NJ). In the *in vitro* experiments, each chemical was dissolved in dimethyl sulfoxide (DMSO) and diluted to their indicated concentrations with the medium (e.g., final concentration, 20 μM H89 or 5 μM KT5720). In the *in vivo* experiments, each chemical was dissolved in vehicle consisting of 5% DMSO (Sigma), 7% dimethyl-acetoacetamide (DMA) (Sigma) and 10% Cremophor El (Sigma) and 77% corn oil (Sigma). All the other chemicals were purchased from Sigma unless otherwise specified. The PTHrP (1-34) peptides were synthesized from GLBiochem China (Shanghai, China). The PTHrP (1–34) ELISA kit was purchased from Phoenix Pharmaceuticals Inc (S-1227, Belmont CA, USA). The neutralizing anti-PTHrP antibody (#MABN793) was purchased from Millipore (Millipore, Bedford, MA, USA). Normal mouse IgG (sc-2025) was used as a control and obtained from Santa Cruz Biotechnology (Santa Cruz CA, USA). The other primary antibodies included anti-UCP1 (Abcam, ab23841; ab10983), anti-OXPHOS (Abcam, ab110413), anti-phospho-CREB (CST, #4276S), anti-total CREB (CST, #9197), anti- phospho-HSL (Ser660) (CST, #4126), anti-total HSL (CST, #4107), anti-phospho-(Ser/Thr) PKA Substrate (CST, #9621), anti-N-cadherin (CST, #13116), anti-vimentin (CST, #5741), anti-E-cadherin (CST, #3195), anti-Ki67 (Abcam, ab16667), anti-mCherry (Abcam, ab167453), anti-GFP (CST, #2956), anti-PAX8 (CST, #59019), anti-Perilipin1 (CST, #9349), anti-CD36 (Absin, abs120668), anti-PTHR (Absin, abs135215), anti-PKA-Cα/β (Abcam, ab71764), anti-PTHLH (Absin, abs136052), anti-MCT1 (Absin, abs120479), anti-MCT4 (Absin, abs135215), anti-β-tubulin (CST, #2146), anti-HSP90 (CST, #4874), anti-α-Actinin (CST, #6487), anti-GAPDH (CST, #5174).

Cell proliferation assay

5-Ethynyl-2-deoxyuridine EdU assay (Beyotime, Shanghai, China) was used to determine the cell proliferative capacity, following the manufacturer's protocol. In brief, the proliferating 786-O or RCC10 cells were treated with 10 μM EdU working solution for 2 h at 37°C. After that, the cells were fixed with 4% paraformaldehyde for 15 min, incubated with 0.1% Triton-X100 for 10 min and stained with DAPI for 10 min. The images were taken with a fluorescence microscope (Olympus, Tokyo, Japan). The number of EdU positive cells was analyzed by ImageJ (Schneider et al., 2012).

Trans-well assays

For migratory assays, 786-O and RCC10 cells were cultured in serum-free medium overnight. Then, cells were seeded in the top chamber of noncoated membrane (8-μm pore size; Corning, NY, USA) and allowed to migrate through the membrane pores. Next, 786-O or RCC10 cells were treated as indicated. Then the migrating cells were fixed in 4% paraformaldehyde for 10 min, followed by washing with PBS three times. The membrane was then stained with 0.5% crystal violet solution for 10 min, followed by washing with PBS three times. Non-migrating cells on the upper side of membrane surface were wiped off with a cotton swab. The membrane was air-dried and then photographed with a light microscope (Olympus, Tokyo, Japan). The number of migrated cells was quantified by ImageJ.

Histological evaluation and immunohistochemistry

For histological examination, tissues as indicated were harvested, fixed with 4% paraformaldehyde in PBS, embedded into paraffin blocks, sectioned (5 μm) and then stained with H&E (Sigma) following standard protocol. Bright-field images were acquired using a microscope (OLYMPUS BX51, Japan). For adipocyte size quantification, Adiposoft software (NIH, Bethesda, MD) was used for analysis following previous protocol (Galarraga et al., 2012). For immunohistochemistry (IHC) analysis, deparaffinized sections were incubated with primary anti-UCP1 antibody (1:200, Abcam) at 4°C overnight, and then incubated species-appropriate secondary antibodies (1:500, Jackson). The images were taken with an inverted microscope (Olympus, Tokyo, Japan).

Immunofluorescence

For fluorescent multiplex immunohistochemistry (mIHC) analysis, a five-color fluorescence kit based on tyramide signal amplification (TSA) were used following the manufacturer's protocol (abs50013, Absin Bioscience, China) (Zhang et al., 2017). In brief, tissue

sections were incubated with primary antibodies as described in the above IHC protocol in two or three sequential cycles before application of corresponding secondary antibodies (PerkinElmer) and TSA solution for AlexaFluor488, AlexaFluor555, AlexaFluor594 and AlexaFluor647, respectively. The following primary antibodies were used: anti-Ki67 (1:200, Abcam), anti-PAX8 (1:200, CST), anti-UCP1 (1:2000, Abcam), anti-Perilipin1 (1:200, CST), anti-GFP (1:200, CST), anti-mCherry (1:400, Abcam). After the last TSA cycle, DAPI was counterstained at a dilution of 1:1000 for 10 min. Fluorescent images (300 ms exposure time) were obtained with an AxioImager.Z2 microscope (Carl Zeiss, Germany).

RNA isolation and RT-qPCR
Total RNA was extracted from frozen tissues or cultured cells using Trizol reagent (Invitrogen, Carlsbad, CA, USA) and then underwent reverse transcription and analyzed by RT-qPCR using commercial kits (Vazyme Biotech, Nanjing, China) (Wei et al., 2020). Reactions were conducted in the 384-well format with a LightCycler 480 II Instrument (Roche Diagnostics, Mannheim, Germany) and relative mRNA abundance was normalized to ribosomal 18S RNA or cyclophilin A using $2\text{-}\Delta\Delta C_t$ method. Primer sequences used are listed in Tables S2 and S3.

Western blotting
Total protein from cells or tissues was harvested with ice-cold RIPA buffer (10 mM Tris, 150 mM sodium chloride, 0.5% sodium deoxycholate, 1% Triton X-100, 0.1% SDS, 1% NP-40, pH 7.4) plus protease inhibitor cocktail (Thermo Fisher Scientific) and phosphatase inhibitor cocktail (Roche). Equivalent amounts of protein were separated on 10% or 12% SDS-PAGE, transblotted onto 0.22-μm PVDF membrane (Merckmillipore, Burlington, MA, USA). Membranes were blocked with 5% skimmed milk (w/v) in TBST buffer for 1 h and incubated with the indicated primary antibodies with gentle rocking overnight at 4°C. Membranes were further incubated with the corresponding HRP-conjugated secondary antibodies (Jackson, 1:5000) for 1.5 h at room temperature. Finally, protein bands were imaged using enhanced chemiluminescence detection kit (Pierce ECL Plus, Thermo Scientific) and analyzed with a luminescent image analyzer (ImageQuant LAS 4000 or Amersham Imager 600, GE Healthcare Life Sciences).

Plasmid constructs and lentivirus preparation
For silencing specific genes, lentiviral-based shRNA constructs in the pLKO.1 vector were obtained from The RNAi Consortium library (Broad Institute, MIT and Harvard, Cambridge, MA, USA). For engineering target gene KO cell clones using CRISPR/Cas9 system, all sgRNAs were designed according to the website (https://tools.synthego.com/) and cloned into the lenti-CRISPR-V2 plasmids (Addgene) (Sanjana et al., 2014). The pCDH plasmids with the reporter genes mCherry or GFP (Addgene) were used for labeling the 786-O and BAC cells, respectively. For lentivirus production, plasmids were prepared using the commercial Endofree plasmid purification kit (QIAGEN) and packaged into viral particles following manufacturer's protocol. Briefly, lentiviruses were produced in 293T cells (ATCC, sex: female) by transient co-transfecting three plasmids including the lentiviral vector, psPAX2, and pMD2.G. At 48 h post-transfection, virus-containing supernatants were harvested, clarified by centrifugation at 800xg for 10 min, filtered through 0.45-μm filters and used directly for transduction of tumor cells or BAC. Then the transduced cells were selected by flow cytometry (FACS Calibur, BD Biosciences, Franklin Lakes, CA, USA) or puromycin (Sigma, final centration of 2 μg/mL).

Determination of lactate content
Brown and white fat pads or differentiated mature adipocytes treated with or without PTHrP (50 ng/mL) were cultured in 12-well plates for 3 h or 24 h in serum-free DMEM. Then the cellular supernatants were collected, and the lactate concentration was measured using colorimetric L-lactate assay kit (Nanjing Jiancheng Bioengineering Institute, Nanjing, China) according to the manufacturer's instructions.

Measurements of lipolysis *in vitro*
Lipolytic activities were assessed by measuring glycerol and FFA release as previously described (Yuan et al., 2017; Li et al., 2015). In brief, fully differentiated mature adipocytes were cultured in a 24-well plate in serum-free DMEM, with or without PTHrP (50 or 100 ng/mL) or H89 (20 μM) for 3 h, and the medium in each well was collected for lipolytic measurement. Extracellular glycerol was extracted and measured by EnzyChrom Adipolysis Assay Kit (BioAssay Systems, Hayward, CA, USA) following the manufacturer's instructions. FFA levels were assessed by enzymatic colorimetric method (LabAssayTM NEFA, Wako, Tokyo, Japan) according to manufacturer's instructions. Glycerol and FFA levels were normalized to total cellular protein amount using the BCA protein assay (Thermo Fisher Scientific).

Measurement of mitochondrial copy number
Total DNA was isolated from tumor-adjacent adipose tissues and distal adipose tissues of ccRCC patients with the EasyPure Genomic DNA Kit (Transgene, China) according to the manufacturer's instructions. DNA concentrations were assessed with a Nanodrop 2000 (Thermo Fisher Scientific) and diluted to final concentrations of 5 ng/mL with ddH$_2$O. mtDNA copy number relative to genomic DNA content was quantified with a LightCycler 480 II Instrument (Roche Diagnostics, Mannheim, Germany). Primer sequences for COX II and β-globin were as follows COX II: (forward) GCCGACTAAATCAAGCAACA, (reverse) CAATGGGCATAAAGC-TATGG; and β-globin: (forward) GAAGCGATTCTAGGGAGCAG, (reverse) GGAGCAGCGATTCTGAGTAG.

MitoTracker staining

Mature adipocytes differentiated from C3H10T1/2 cells were treated with DMSO or PTHrP (50 ng/mL) for 24 h. Cells were cultured with pre-warmed medium containing 200 nM MitoTracker Red probe (Invitrogen) for 30 min and then washed twice with fresh medium. Cells images were immediately captured with a fluorescence microscope (Nikon) after staining.

Seahorse XFe96 measurements

The Seahorse Bioscience XF(e)96 Flux Analyzer Agilent Technologies) was used to measure the OCR or ECAR of mature adipocytes and tumor cells according to the manufacturer's protocol (Calton et al., 2016). In brief, C3H10T1/2 cells were differentiated for 5 days and seeded at a density of 3.5×10^3 cells/well into 96-well plates and allowed for adherent to the bottom overnight, followed by treatment with the corresponding CM (from HK2 cells or 786-O cells or RCC10 cells) or PTHrP for additional 24 h. The mitochondrial stress test utilizes sequential injections of oligomycin (4.5 μM), Carbonyl cyanide 4-(trifluoromethoxy) phenylhydrazone (2 μM, FCCP), and rotenone/antimycin A in combination (1 μM). The parameters of basal respiration, uncoupled respiration and maximal respiration were automatically calculated by the WAVE software (Agilent). For measuring EACR, the glycolytic stress test utilizes sequential injections of glucose (10 mM), oligomycin (4.5 μM), and 2-deoxyglucose (50 mM, 2DG). To eliminate the influence caused by mitochondrial-derived CO_2, we performed seahorse assay with the Seahorse XF Glycolytic Rate Assay kit (103344–100, Agilent Technologies) and the basal OCR and ECAR were measured followed by injecting rotenone/antimycin A (2 μM) and 2-DG (50 mM) sequentially. The proton efflux rates of glycolysis (glycoPER) were automatically calculated by the WAVE software (Agilent). For detecting lactate-dependent OCR, 786-O cells were seeded at a density of 5×10^3 cells/well into 96-well plates and allowed for adhesion overnight. Cells were incubated in XF assay medium (containing 10 mM glucose and 2 mM L-glutamine) for 1 h without CO_2 before oxygen consumption analysis. After basal measurement, various concentration of lactate (1 mM-15 mM) was injected into the wells and lactate-induced OCR were detected for 5 cycles followed by 7ACC1 (10 μM) addition. To determine OCR from FAO, HK2, 786-O and RCC10 cells were seeded at a density of 5×10^3 cells/well into and allowed for adhesion overnight. OCR of the above cells were measured under basal condition for 4 cycles and after administrating the cells with the inhibitor of FAO rate-limiting gene CPT1α (Eto, 2 μM). All parameters were normalized to total protein amount in individual wells using the BCA protein assay (Thermo Fisher Scientific).

Metabolic flux assay

786-O cells were seeded in 15 cm diameter petri-dishes with DMEM (high glucose) (Gibco) containing 10% FBS, 100 U/mL penicillin, and 100 μg/mL streptomycin and were cultured in 37°C with 5% CO_2. After 24 h incubation, media were removed and cells were washed with PBS for three times before the addition of DMEM (without glucose) supplemented with 10 mM label-free glucose and 5 mM label-free lactate or [U-$^{13}C_3$]-lactate (Cambridge Isotope Laboratory, Tewksbury, MA). Media and cells were then collected after extra 24 h incubation. For metabolite extraction, cells were homogenized with 600 μL cold methanol aqueous solution ($V_{methanol}$: V_{water} = 5:1, -20°C, overnight), then the cells were lysed by three freeze-thaw cycles and ultrasonication-break (1 min each) for eight cycles in an ice-bath (Wu et al., 2014), and supernatant were collected after centrifugation (12000xg, 4°C, 10min). The remaining pellets were further extracted twice with the same procedure. The supernatants were pooled together. Media extracts were clarified with 2 volumes of cold methanol (-20°C, overnight) to precipitate the protein, and then centrifuged (1600xg, 10 min) to collect supernatant. For measurement of lactate-derived metabolites, the supernatants of cell or media extracts were lyophilized, and the powders of extracts were re-dissolved in 600 μL phosphate buffer in D_2O (0.1M, pD7.4) for Q-1D-HMBC and completely relaxed ^{1}H-NMR spectra analysis (Wan et al., 2017; Dai et al., 2010). For measurement of intermediates in TCA cycle by mass spectrometry, the lyophilized samples after NMR analysis were redissolved in 100 μL 50% aqueous methanol respectively.

NMR and UPLC-ESI-MS/MS analysis

All NMR spectra were obtained at 298K on a Bruker Avance III 600 MHz NMR spectrometer (operating at 600.13 MHz for ^{1}H) equipped with an inverse cryogenic probe. For the NMR-based metabolic flux analysis of cell and medium samples, K_2HPO_4 and NaH_2PO_4 were employed to prepare the phosphate buffer (0.1 M, pD 7.4) in D_2O containing 0.1% NaN_3 (w/v) and 7.725 mM TSP (as internal standard) for optimal solubility and buffering capacity (Xiao et al., 2009). All one-dimensional ^{1}H-NMR spectra were manually corrected for phase and baseline using TOPSPIN software with chemical shift referenced to the TSP signal (δ0.00). The resonances were assigned to specific metabolites based on the in-house developed databases. Peak deconvolution and integration were performed using MestReNova (V8.1.0, Mestrelab Research S. L.).

LC-MS data were acquired on a Waters ACQUITY UPLC Xevo G2-XS QTOF (Waters, Milford, USA) with ESI ion source in the negative ion mode. Each sample (1 μL) was analyzed using a Waters BEH C18 column (2.1*100 mm, 1.7 μm) at 40 $^\circ$C with mobile phase A (0.1% formic acid in water) and mobile phase B (0.1% formic acid in methanol) with a flow rate of 0.35 mL/min. An optimized chromatographic method was established and the elution gradient was used as follows: 0-1min, 2%B; 1-3min, 2%-15% B; 3-4 min, 15%-50%B; 4-5min, 50%-95%B; 5-8min, 95%B; 8-8.1min, 95%-2%B, 8.1-12min, 2%B. MS was scanned from 50 Da to 1200 Da with scan mode. The capillary voltage was 1.5 kV. Sampling cone gas flow rate was 50 L/h with 30 V voltage. The source temperature and desolvation temperature were 120 $^\circ$C and 500 $^\circ$C, respectively. Desolvation gas flow rate was 800 L/h. Metabolite identification was confidently ensured by matching the precursor ions, product ions, and retention times with the corresponding standard compounds.

Lung metastasis assay

For lung metastasis model, 1 x 10^6 Luc-expressing 786-O cells were injected into the tail vein of BALB/c nude mice (aged 4 to 6 weeks, GemPharmatech). The progression of metastases was monitored 6 and 8 weeks later by bioluminescent (BL) imaging using the IVIS@ Lumina II system (Caliper Life Sciences, Hopkinton, MA) 10 min after intraperitoneal injection of 100 μL of D-luciferin (15 mg/mL). Mice were euthanized, and lungs were harvested for monitoring the metastases by the IVIS@ Lumina II system (Caliper Life Sciences, Hopkinton, MA) and then were subjected to 4% paraformaldehyde for the subsequent hematoxylin-eosin staining. For lung nodules analysis, a minimum of three sections were excised at 100 μm intervals and metastases in each section were counted manually on an AxioImager.Z2 microscope (Carl Zeiss, Germany).

Orthotopic tumor growth

Male BALB/c nude mice (aged 4 to 6 weeks, GemPharmatech) were anesthetized and placed in a lateral position (right side down) for orthotopic xenograft studies as described previously (Qu et al., 2016). Briefly, a skin incision (5- to 7- mm) was made and the abdominal cavity was opened along the left flank of the mouse. Then the left kidney was pushed out with gentle pressure by two fingers. For orthotopic injection, 2 x 10^6 Luc-expressing 786-O cells were resuspended in 20 μL PBS and injected orthotopically into the subcapsular space of the left kidney. After injection, a sterile cotton tip was used to prevent leakage of tumor cells and local bleeding. Then, the abdomen and the skin were in turn closed with a re-absorbable suture. To monitor tumor growth, the mice were imaged after 6 and 8 weeks by bioluminescence using the IVIS@ Lumina II system (Caliper Life Sciences, Hopkinton, MA, USA) 10 min after intraperitoneal injection of 100 μL of D-luciferin (15 mg/mL). Mice were then euthanized, and lungs were harvested for monitoring metastases using the IVIS@ Lumina II system (Caliper Life Sciences) and then fixed with 4% paraformaldehyde for subsequent hematoxylin-eosin staining. For lung nodule analysis, a minimum of three sections were excised at 100 μm intervals, and metastases in each section were counted manually on an AxioImager.Z2 microscope (Carl Zeiss, Germany).

QUANTIFICATION AND STATISTICAL ANALYSIS

All data were presented as the means ± standard error of mean (SEM) unless otherwise described. The normality of data distribution was analyzed by Shapiro-Wilk test and Kolmogorov-Smirnov test. Normally distributed data were statistically analyzed using unpaired two-tailed Student's t tests or paired t tests or One-way analysis of variance (ANOVA) or Two-way ANOVA using GraphPad Prism 7.0 software. Non-normally distributed data were analyzed using non-parametric test. The data from TCGA database were analyzed with Statistics::TTest or log-rank test as previously described (Chandrashekar et al., 2017). $p < 0.05$ was considered as statistically significant. The mice were randomly distributed into different groups in all experiments. Experiments of imaging and histology were also performed in a blinded fashion. The sample size in each study was based on experience with previous studies in our lab (Chen et al., 2021). No data points were excluded from the study.